



Defense Threat Reduction Agency
8725 John J. Kingman Road, MS
6201 Fort Belvoir, VA 22060-6201



DTRA-TR-17-4

TECHNICAL REPORT

Study of Radiation Hardness of Lattice Matched AlInN/GaN HEMT Heterostructures

Distribution Statement A. Approved for public release; distribution is unlimited.

October 2016

HDTRA1-11-1-0071

Patrick Kung

Prepared by:
University of Alabama
Department of Electrical and
Computer Engineering
Tuscaloosa, AL 35487

DESTRUCTION NOTICE:

Destroy this report when it is no longer needed.
Do not return to sender.

PLEASE NOTIFY THE DEFENSE THREAT REDUCTION
AGENCY, ATTN: DTRIAC/ J9STT, 8725 JOHN J. KINGMAN ROAD,
MS-6201, FT BELVOIR, VA 22060-6201, IF YOUR ADDRESS
IS INCORRECT, IF YOU WISH IT DELETED FROM THE
DISTRIBUTION LIST, OR IF THE ADDRESSEE IS NO
LONGER EMPLOYED BY YOUR ORGANIZATION.

REPORT DOCUMENTATION PAGE					Form Approved OMB No. 0704-0188	
<p>The public reporting burden for this collection of information is estimated to average 1 hour per response, including the time for reviewing instructions, searching existing data sources, gathering and maintaining the data needed, and completing and reviewing the collection of information. Send comments regarding this burden estimate or any other aspect of this collection of information, including suggestions for reducing the burden, to Department of Defense, Washington Headquarters Services, Directorate for Information Operations and Reports (0704-0188), 1215 Jefferson Davis Highway, Suite 1204, Arlington, VA 22202-4302. Respondents should be aware that notwithstanding any other provision of law, no person shall be subject to any penalty for failing to comply with a collection of information if it does not display a currently valid OMB control number.</p> <p>PLEASE DO NOT RETURN YOUR FORM TO THE ABOVE ADDRESS.</p>						
1. REPORT DATE (DD-MM-YYYY) 00-10-2016		2. REPORT TYPE Technical		3. DATES COVERED (From - To) 8/25/11-8/24/15		
4. TITLE AND SUBTITLE Study of Radiation Hardness of Lattice Matched AlInN/GaN HEMT Heterostructures				5a. CONTRACT NUMBER		
				5b. GRANT NUMBER HDTRA-1-11-1-0071		
				5c. PROGRAM ELEMENT NUMBER		
6. AUTHOR(S) Patrick Kung				5d. PROJECT NUMBER		
				5e. TASK NUMBER		
				5f. WORK UNIT NUMBER		
7. PERFORMING ORGANIZATION NAME(S) AND ADDRESS(ES) University of Alabama Department of Electrical and Computer Engineering Tuscaloosa, AL 35487				8. PERFORMING ORGANIZATION REPORT NUMBER		
9. SPONSORING/MONITORING AGENCY NAME(S) AND ADDRESS(ES) Defense Threat Reduction Agency 8725 John J. Kingman Road Fort Belvoir, VA 22060-6201				10. SPONSOR/MONITOR'S ACRONYM(S) DTRA		
				11. SPONSOR/MONITOR'S REPORT NUMBER(S) DTRA-TR-17-4		
12. DISTRIBUTION/AVAILABILITY STATEMENT Distribution Statement A. Approved for public release; distribution is unlimited.						
13. SUPPLEMENTARY NOTES						
14. ABSTRACT <p>This project was concerned with the development of atom probe tomography for the correlated analysis of the effects of radiation exposure on the nanostructural characteristics of strain-free, lattice-matched AlInN/GaN based high electron mobility transistor heterostructures and devices, and in comparison to strained AlGaIn/GaN structures. Better basic fundamental understanding of such effects can help the development of GaN based electronics that are resistant to radiation environments of interest to the Defense Threat Reduction Agency. This project was part of the field of wide bandgap high power, high frequency electronics, as well as fundamental materials science of these materials.</p>						
15. SUBJECT TERMS atom probe tomography, gallium nitride, aluminum indium nitride, high electron mobility transistor						
16. SECURITY CLASSIFICATION OF:			17. LIMITATION OF ABSTRACT	18. NUMBER OF PAGES	19a. NAME OF RESPONSIBLE PERSON	
a. REPORT	b. ABSTRACT	c. THIS PAGE			Jacob Calkins	
Unclassified	Unclassified	Unclassified	UU	35	19b. TELEPHONE NUMBER (Include area code) 703-767-3075	

UNIT CONVERSION TABLE

U.S. customary units to and from international units of measurement*

U.S. Customary Units	<div style="display: flex; align-items: center; justify-content: center;"> <div style="margin-right: 10px;"> </div> Multiply by </div> <div style="display: flex; align-items: center; justify-content: center;"> <div style="margin-right: 10px;"> </div> Divide by† </div>	International Units
Length/Area/Volume		
inch (in)	2.54 $\times 10^{-2}$	meter (m)
foot (ft)	3.048 $\times 10^{-1}$	meter (m)
yard (yd)	9.144 $\times 10^{-1}$	meter (m)
mile (mi, international)	1.609 344 $\times 10^3$	meter (m)
mile (nmi, nautical, U.S.)	1.852 $\times 10^3$	meter (m)
barn (b)	1 $\times 10^{-28}$	square meter (m ²)
gallon (gal, U.S. liquid)	3.785 412 $\times 10^{-3}$	cubic meter (m ³)
cubic foot (ft ³)	2.831 685 $\times 10^{-2}$	cubic meter (m ³)
Mass/Density		
pound (lb)	4.535 924 $\times 10^{-1}$	kilogram (kg)
unified atomic mass unit (amu)	1.660 539 $\times 10^{-27}$	kilogram (kg)
pound-mass per cubic foot (lb ft ⁻³)	1.601 846 $\times 10^1$	kilogram per cubic meter (kg m ⁻³)
pound-force (lbf avoirdupois)	4.448 222	newton (N)
Energy/Work/Power		
electron volt (eV)	1.602 177 $\times 10^{-19}$	joule (J)
erg	1 $\times 10^{-7}$	joule (J)
kiloton (kt) (TNT equivalent)	4.184 $\times 10^{12}$	joule (J)
British thermal unit (Btu) (thermochemical)	1.054 350 $\times 10^3$	joule (J)
foot-pound-force (ft lbf)	1.355 818	joule (J)
calorie (cal) (thermochemical)	4.184	joule (J)
Pressure		
atmosphere (atm)	1.013 250 $\times 10^5$	pascal (Pa)
pound force per square inch (psi)	6.984 757 $\times 10^3$	pascal (Pa)
Temperature		
degree Fahrenheit (°F)	$[T(^{\circ}\text{F}) - 32]/1.8$	degree Celsius (°C)
degree Fahrenheit (°F)	$[T(^{\circ}\text{F}) + 459.67]/1.8$	kelvin (K)
Radiation		
curie (Ci) [activity of radionuclides]	3.7 $\times 10^{10}$	per second (s ⁻¹) [becquerel (Bq)]
roentgen (R) [air exposure]	2.579 760 $\times 10^{-4}$	coulomb per kilogram (C kg ⁻¹)
rad [absorbed dose]	1 $\times 10^{-2}$	joule per kilogram (J kg ⁻¹) [gray (Gy)]
rem [equivalent and effective dose]	1 $\times 10^{-2}$	joule per kilogram (J kg ⁻¹) [sievert (Sv)]

* Specific details regarding the implementation of SI units may be viewed at <http://www.bipm.org/en/si/>.

† Multiply the U.S. customary unit by the factor to get the international unit. Divide the international unit by the factor to get the U.S. customary unit.

Contents

1. Project Objective, Approach and Scope	3
2. Technical Accomplishments / Findings.....	3
2.1. HEMT Heterostructure Growth and Fabrication	3
2.2. Atom Probe Tomography Specimen Preparation Challenges and Remediation	4
2.3. Atom Probe Tomography Measurement and Analysis Challenges	6
2.4. Gamma Ray Irradiation of AlInN/GaN & AlGaIn/GaN HEMT Structures	8
2.4.1. Characterization of Irradiated AlInN/GaN and AlGaIn/GaN HEMT Heterostructures.....	8
2.4.2. APT of Baseline Un-Irradiated Lattice Matched AlInN/GaN HEMT Heterostructures	9
2.4.3. APT of Gamma-Irradiated Lattice Matched AlInN/GaN HEMT Heterostructures	11
2.4.4. Proxigram Comparison of Un-Irradiated and Gamma Irradiated AlInN/GaN HEMT Heterostructures	13
2.4.5. APT of Un-Irradiated and Gamma Irradiated Strained AlGaIn/GaN HEMT Heterostructures	13
2.4.6. Electrical Characteristics of Un-Irradiated and Irradiated AlInN/GaN & AlGaIn/GaN HEMTs ..	15
2.4.7. Summary	17
2.5. Proton Irradiation of AlInN/GaN & AlGaIn/GaN HEMT Structures	17
2.5.1. Design of Proton Irradiation Experiments.....	18
2.5.2. Effect on Electrical Transport Characteristics of AlInN/GaN and AlGaIn/GaN HEMT Structures	19
2.5.3. Atom Probe Tomography Analysis of Proton Irradiated Structures	20
2.5.4. Correlated Analysis of Proton Irradiation on AlInN/GaN and AlGaIn/GaN HEMT Structures	23
2.5.5. Effect of Room Temperature and Low Temperature Photoluminescence Characteristics.....	25
2.5.6. Investigation of Indium Clustering Using APT	27
2.6. Development of Low Temperature AlN Dielectric Passivation Layer	28
3. Impact	31
3.1. Training and Professional Development	31
3.2. Dissemination	31
3.3. Honors and Awards	31

1. PROJECT OBJECTIVE, APPROACH AND SCOPE

The objective of this project is to gain fundamental understanding of radiation mechanisms in AlInN/GaN based high electron mobility transistor (HEMT) heterostructures and devices. Gaining such basic knowledge can reduce the risk to the development of emerging GaN based electronics that are resistant to nuclear and space radiation effects. This project is part of the field of wide bandgap high power, high frequency electronics, as well as fundamental materials science of these materials.

The technical approach consists of investigating the atom probe tomography (APT) of strain free, lattice matched AlInN/GaN heterostructures and devices after irradiation. APT offers the unique combination of field ion microscopy and time-of-flight spectroscopy to enable the 3D reconstruction map of elements in a structure with theoretically chemical isotope resolution capability and atomic spatial resolution. As such, atom probe tomography is potentially uniquely capable of identifying radiation induced defects in the electronic materials of interest.

In this project, we specifically plan to: (1) investigate buried interface roughening near the channel and alloy composition fluctuation in 3D before and after irradiation; (2) investigate metal-semiconductor (gate) and passivation layer-semiconductor interfaces before and after irradiation; (3) compare AlGaIn/GaN and lattice matched AlInN/GaN heterostructures; (4) compare AlGaIn/GaN and lattice matched AlInN/GaN HEMT DC characteristics before and after irradiation; (5) irradiate our specimens with total dose ^{60}Co and protons.

2. TECHNICAL ACCOMPLISHMENTS / FINDINGS

2.1. HEMT Heterostructure Growth and Fabrication

The HEMT structures studied in this project were grown by metalorganic vapor phase epitaxy (MOVPE). Lattice matched $\text{Al}_{0.83}\text{In}_{0.17}\text{N}/\text{GaN}$ HEMT heterostructures utilized the lattice matching conditions for AlInN and had the general structure shown in Figure 1(a), consisting of a thin (2 nm) GaN contact layer, on a 10 nm $\text{Al}_{0.83}\text{In}_{0.17}\text{N}$ barrier layer on a 2.0 μm thick semi-insulating GaN template. A thin (1 nm) AlN interlayer was inserted between the AlInN barrier and the channel material to enhance carrier confinement. An AlN buffer layer was grown directly on basal plane sapphire prior to the high resistivity of the GaN template layer. These structures typically yielded a typical sheet carrier density of $2\sim 3\times 10^{13} \text{ cm}^{-2}$ and a mobility of $650\sim 700 \text{ cm}^2/\text{Vs}$ at room temperature.

As a baseline for comparison, similar but strained $\text{Al}_{0.25}\text{Ga}_{0.75}\text{N}/\text{GaN}$ HEMT heterostructures were also realized by MOVPE on basal plane sapphire substrates. The structures were similar with the thickness of the $\text{Al}_{0.25}\text{Ga}_{0.75}\text{N}$ barrier layer being 25 nm, as shown in Figure 1(b). These structures typically yielded a sheet carrier density of $1\sim 2\times 10^{13} \text{ cm}^{-2}$ and a mobility of $\sim 1400 \text{ cm}^2/\text{Vs}$ at room temperature.

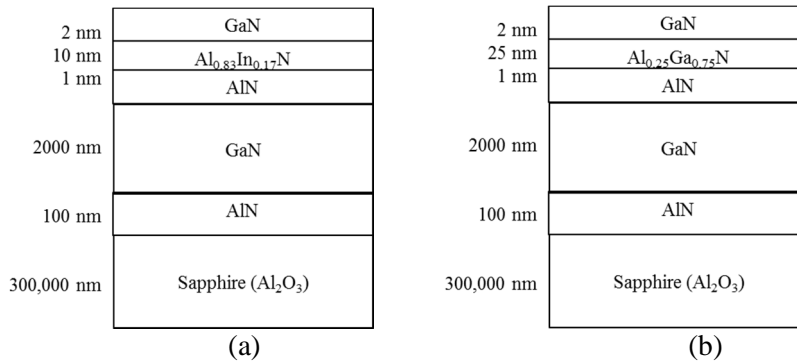


Figure 1. Schematic of the AlInN/GaN and AlGaIn/GaN HEMT structures investigated.

In addition the heterostructure wafers, HEMT devices were fabricated. A photomask was designed and acquired, with the layout shown in Figure 2. Several gate lengths were available, ranging from 2 to 3 μm . Mesas were first etched in the wafer to isolate individual transistors by ion milling. This was followed by successively conducting photolithography steps and the deposition of Ti/Au ohmic contacts for the source and drain, as well as Schottky Ni/Au contacts for the gate by electron beam evaporation. Final metal contact pads were evaporated for probing.

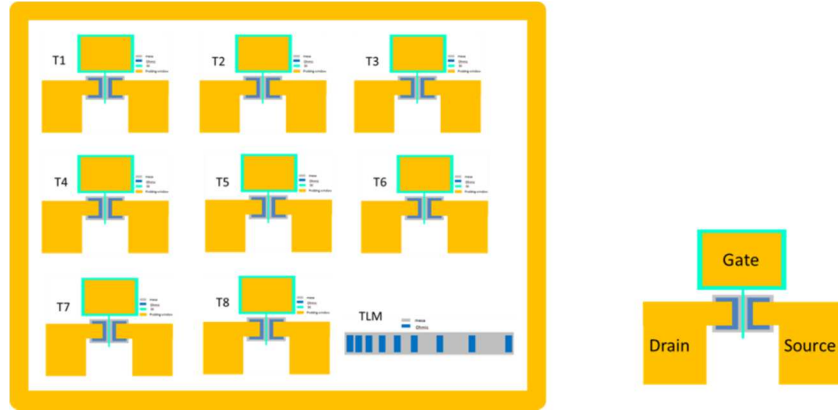


Figure 2. Photomask layout used for AlInN/GaN and AlGaIn/GaN HEMTs.

2.2. Atom Probe Tomography Specimen Preparation Challenges and Remediation

In general, atom probe tomography experiments necessitate the realization of needle-shaped specimens of approximately 80~100 nm or less in diameter that contains the region of interest near the apex of the tip in order to achieve field ion emission under high bias in a vacuum. The general specimen preparation process we had been using involves using a dual beam focused ion beam (FIB) to accomplish the following steps, as illustrated in the series of scanning electron microscopy (SEM) images in Figure 3:

- a- Defining and deposition of a rectangular Pt capping protective layer deposited by FIB.
- b- Milling a rectangular wedge around the region of interest, with a triangular cross-section.
- c- Attachment of the wedge to a nanomanipulator probe.
- d- Lifting-out of the wedge from the bulk sample.
- e- Attachment of a portion of the wedge to one of the silicon posts on a micro-tip array.
- f- Slicing of the wedge to leave the raw specimen.
- g- Annular milling of attached portion of the wedge into the desired needle shape.

In the case of the AlInN/GaN and AlGaIn/GaN HEMT structures, this presented specific challenges that we identified and were able to overcome as described in this section. They primarily pertained to the need to not ion mill away the region of interest at various stages of the preparation process, i.e. the channel where HEMT channel at the (AlInN or AlGaIn)/GaN interface, which is located only 15 nm from the top surface and is only 10~25 nm thick (Figure 4). Because the HEMT structures were grown on semi-insulating GaN on sapphire substrates, both of which are hard to mill, long and intense (Ga) ion beam milling are needed to cut out a wedge (steps b and g, as illustrated in Figure 4). But this can potentially damage the region of interest, or lead to ion implantation. Our approach to alleviate this issue was to significantly increase the thickness of the metal protective layer, from an original 0.5 μm to 2 μm or more. However, we subsequently found that this protective layer could not be too thick either. Otherwise, the region of interest would be further from the tip apex (shown as red dashed circle in Figure 4 (bottom)), which means that the tip would be blunt by the time it is analyzed during APT experiments.

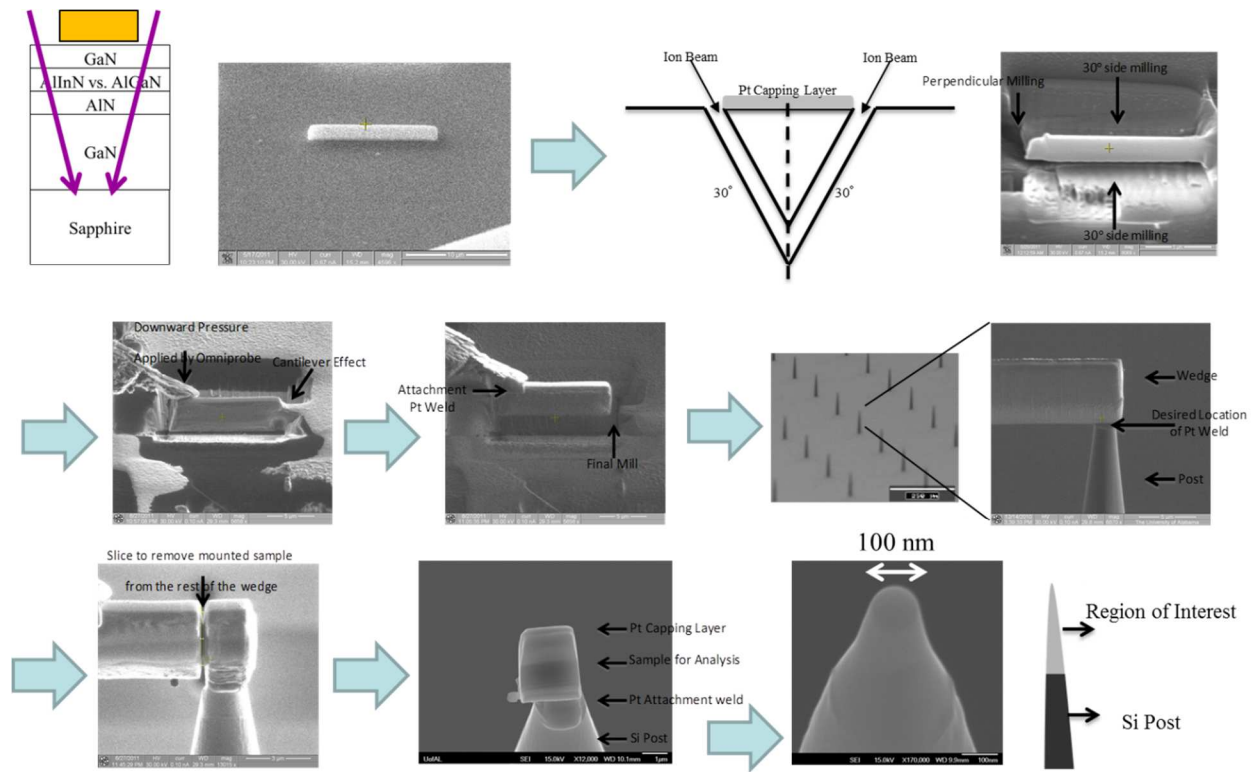


Figure 3. APT specimen preparation steps using focused ion beam, illustrated through scanning electron microscopy images at various steps in the process.

Not only was the thickness of the protective metal layer critical, the way it was deposited was as important. In our optimized process, this layer was not entirely composed of the Pt deposited by FIB because this would have required a long deposition time in the FIB and thus increase in the risk of ion damage to the region of interest. Instead, we chose to use electron beam evaporated Cu metal, which ensured that no implantation damage occurred. The choice of Cu was because of its ease of evaporation at high rates, high electrical conductivity, and low cost. In addition, this created a conductive path that mitigated the sample charging effects that often occurred during our earlier FIB process.

Using our original procedure, we experienced that the success of our APT experiments had been limited because we milled past the channel region most of the time. With the optimized protective metal preparation process, we experienced a dramatic jump in our APT experiment success rate. A typical example of optimized APT specimen tip that we can routinely obtain from both our AlInN/GaN or AlGaIn/GaN heterostructures is shown in Figure 3 with a diameter of ~100 nm and with a shank angle of ~13°.

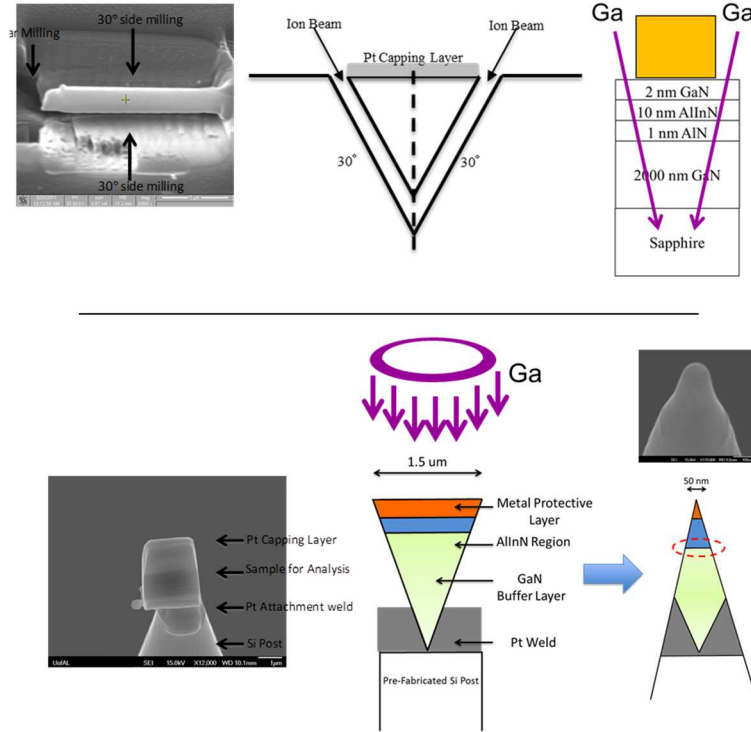


Figure 4. Steps b (top) and g (bottom) of the APT specimen preparation process showing the specific challenges encountered in the case of AlInN/GaN or AlGaIn/GaN based HEMT structures.

2.3. Atom Probe Tomography Measurement and Analysis Challenges

APT measurements are carried out using a Local Electrode Atom Probe (LEAP) 4000X where the specimen tip is cooled down to 40-70 K in vacuum and a high bias (3~11 kV) is applied between it and the local electrode to bring the structure just below the threshold for field ion emission (Figure 5). A pulsed laser (532 nm, 15 ps) brings the additional energy needed to overcome this threshold and evaporate ions from the specimen surface. Ions are then detected in by a position-sensitive detector (imaging detector) that yields the spatial coordinates of the ion original positions in the structure, while the time-of-flight allows identification of their mass-to-charge ratios. Following collection, the data is analyzed post-experiments.

Achieving ion emission from actual AlInN/GaN or AlGaIn/GaN HEMT structures has been challenging because of their highly resistive characteristics, as one can observe in Figure 5. This first leads to a reduced thermal conductivity of the specimen tip and thus an increase in its brittleness at the junction with the silicon post when illuminated by an intense laser pulse. Additionally, the potential difference between the tip apex (i.e. near the region of interest) and the local electrode would be lower than the applied bias, which means that the field ion emission would be less efficient or that a higher bias would need to be applied with an increased risk of arc-ing. Furthermore, this would lead to measurement artifacts because the ions would not be accelerated across the electric field in the manner expected, which complicates analysis of the time-of-flight spectrum. Here again, optimized specimen preparation, especially the annular milling step, was critical in ensuring that the specimen was able to be measured in the APT experiment.

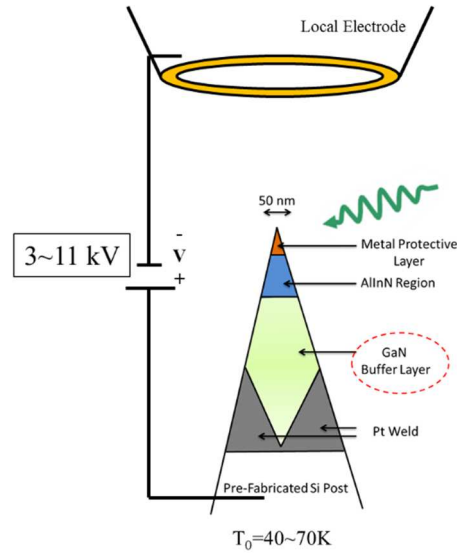


Figure 5. Illustration of the APT experimental measurement.

The brittleness and the potential for arc-ing are believed to be fundamentally at the origin of the main premature failure mechanisms encountered during APT measurements. Figure 6 shows SEM images of the resulting structure either Figure 6(a) after the tip has either broken off the post or Figure 6(b) after arc-ing. One should note from the scale bar that the ~ 100 nm diameter tip apex would merely be a pixel dot in Figure 6, which means that these common failure mechanisms are quite dramatic. When these occur, the atom and molecule species outgassed in the chamber are ionized by the high electric field and lead to an artifact spectrum such as the one shown in Figure 7, where most of the peaks cannot be identified. Eventually, adjustments of the APT measurement parameters, combined with optimized specimen preparation, have been made to overcome these challenges and lead to successful APT analysis of both AlInN/GaN and AlGaIn/GaN HEMT structures. These parameters included the specimen temperature, laser pulse energy and frequency.

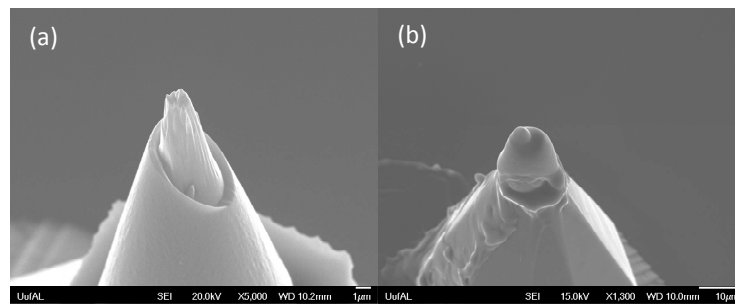


Figure 6. Scanning electron microscopy images of the main failure mechanisms observed under APT: (a) shows the state after the tip has broken under stress, (b) is after the tip has shattered due to the high electric field.

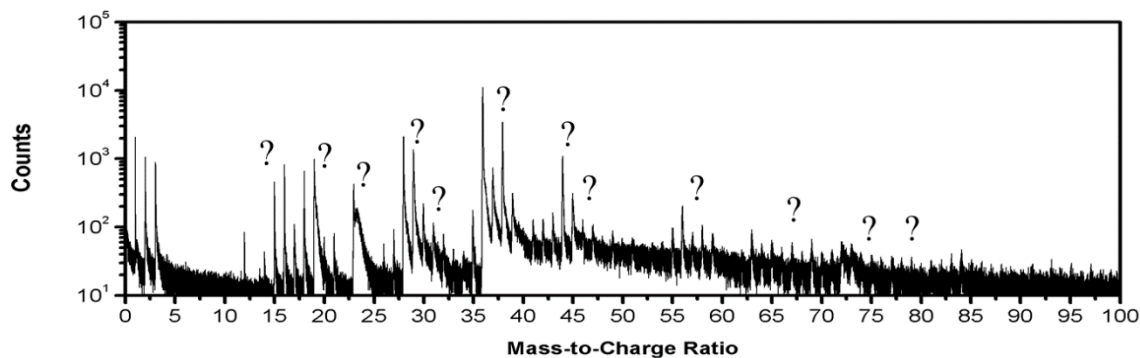


Figure 7. Mass Spectrum originating from a tip that has prematurely failed. Most of the detected peaks are due to ionized atom/molecules outgassed after tip break and not the sample emitting ions.

2.4. Gamma Ray Irradiation of AlInN/GaN & AlGaIn/GaN HEMT Structures

Total dose ^{60}Co gamma irradiation of both AlInN/GaN and AlGaIn/GaN HEMTs has been carried out by subcontractor Scientific, Inc. The exposures were conducted at the Gamma Radiation Facility at NAVSEA Crane division with doses up to ~ 6 Mrad(Si). The transistor DC characteristics were measured at intermediate doses.

2.4.1. Characterization of Irradiated AlInN/GaN and AlGaIn/GaN HEMT Heterostructures

Routine material characterizations of the HEMT structures before and after gamma irradiation were conducted. Atomic force microscopy (AFM) of the topmost surface of the $\text{Al}_{0.83}\text{In}_{0.17}\text{N}/\text{GaN}$ and $\text{Al}_{0.25}\text{Ga}_{0.75}\text{N}/\text{GaN}$ HEMT structures did not yield significant changes from prior to after irradiation beyond measurement statistics. The rms roughness was about 1.617 nm for the AlInN/GaN while it was 0.835 nm for the AlGaIn/GaN. Room temperature photoluminescence was carried out on the structures before and after irradiation, as shown in Figure 8(a) and (b). The dominant peak observed arises from the GaN template layer, and the clear reduction of its emission intensity after irradiation is correlated with an increase of nonradiative recombination centers which annihilate the carriers near the band edge of the materials. Such centers are in turn associated with defects that act as traps and can scatter charge carriers, similar to what was observed in the prior electrical characterizations.

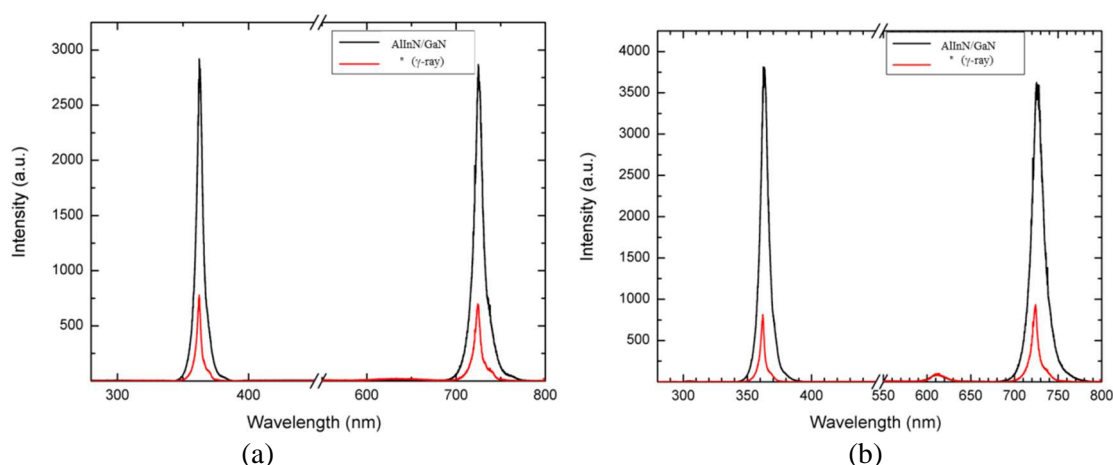


Figure 8. Room temperature photoluminescence from (a) AlInN/GaN and (b) AlGaIn/GaN HEMT structures. The peaks beyond 600 nm are second order diffraction from the spectrograph.

Transmission electron microscopy (TEM) also did not exhibit the minute changes that were only visible by APT. Figure 9(a) shows a typical high resolution cross-section TEM micrograph. Energy

dispersive spectroscopy carried out during scanning TEM yielded alloy concentrations for AlInN and AlGaN that were generally consistent with the APT collected data, however they were more scattered and less accurate because the size of the electron beam interaction volume during TEM can include regions outside of the thin AlInN or AlGaN during analysis. Raman spectroscopy was used to reveal any potential strain change in the structures. The spectra before and after irradiation are shown in Figure 9(b) for both the AlInN/GaN and AlGaN/GaN. No peak shift could be observed under magnification, which suggests that gamma ray is not damaging enough to cause a macroscopically observable change in the strain within the HEMT structures.

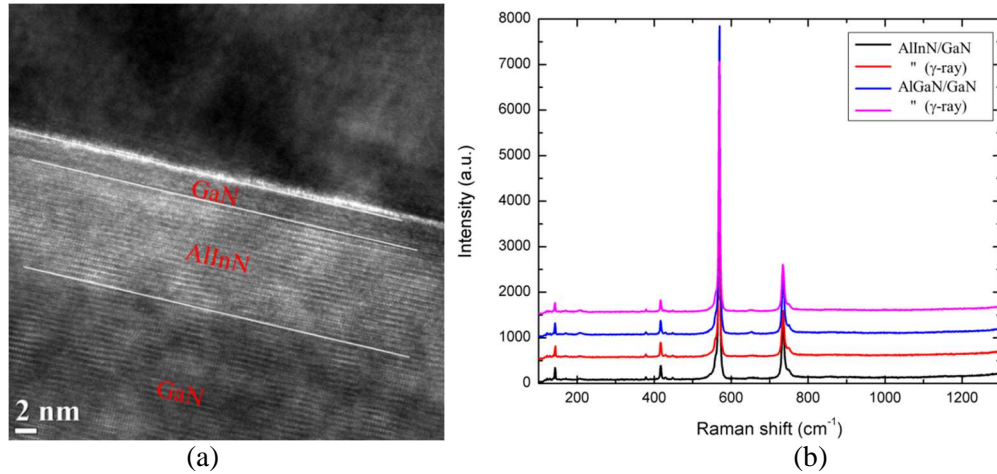


Figure 9. (a) High resolution cross section TEM micrograph of an AlInN/GaN HEMT structure and (b) Raman spectra of both AlInN/GaN and AlGaN/GaN HEMT structures before and after gamma irradiation.

2.4.2. APT of Baseline Un-Irradiated Lattice Matched AlInN/GaN HEMT Heterostructures

APT measurements of un-irradiated lattice matched AlInN/GaN HEMT heterostructures typically yielded the mass spectrum shown in Figure 10 where each count corresponds to detected isotopic species. In the spectrum, all the main peaks have been identified and assigned to the AlInN/GaN. All the constituent elements were observed, with relevant peaks detected assigned to primarily monoatomic (preferred) species Al^{+++} , Al^{++} , Al^{+} , Ga^{++} , Ga^{+} , In^{++} , In^{+} , N^{++} , N^{+} , as well as only few molecular species N_2^{+} , N_3^{+} , and GaN_3^{++} . The challenge in detecting large counts of Al and In comes from the fact that the AlInN layer in HEMT structures is only a few nm thin. Such spectrum is very similar to what we had previously seen with our pure GaN samples, but with additional Al and In peaks associated with AlInN.

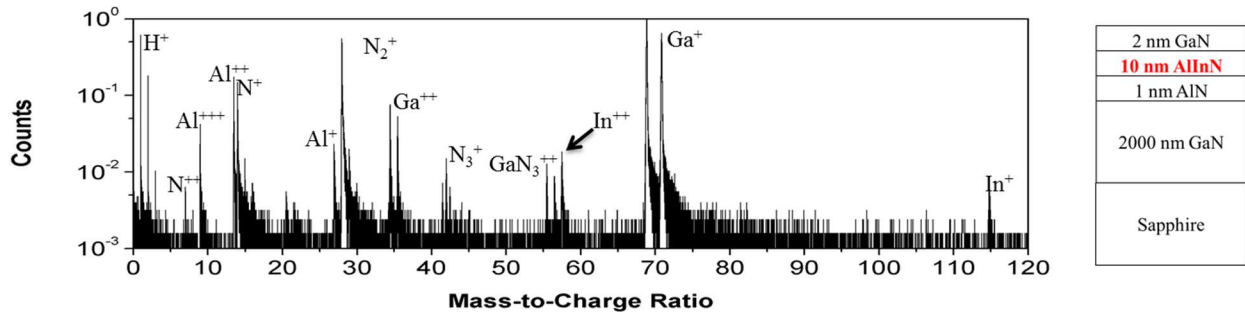


Figure 10. Mass spectrum of the complete AlInN/GaN HEMT structure. All the single ions and a few some compound related peaks inherent to GaN field ion emission are visible.

From the mass spectrum, we were able to achieve 3D reconstructions, as shown in Figure 11 where each of the elements detected is represented by a colored dot. Figure 11(a) represents the full reconstruction of the probed area, with Figure 11(b) showing a up close look of the reconstruction at the region of interest i.e. the channel interface region. Figure 11(c), (d) and (e) are the reconstructions showing only the Al (blue), In (purple), and N related ions (green) from N or compound N_3 and GaN_3 , respectively. We can clearly observe the presence of In and Al in the topmost region, consistent with the expected AlInN/GaN structure. Ga (orange) is also mostly absent from the AlInN layer, except the very top surface which corresponds to the GaN contact layer and confirms that the specimen preparation was optimized enough to prevent damage to the structure during FIB process. Being able to know the position of individual elements throughout the 3D structure enables us to investigate concentration profiles and iso-concentration surfaces.

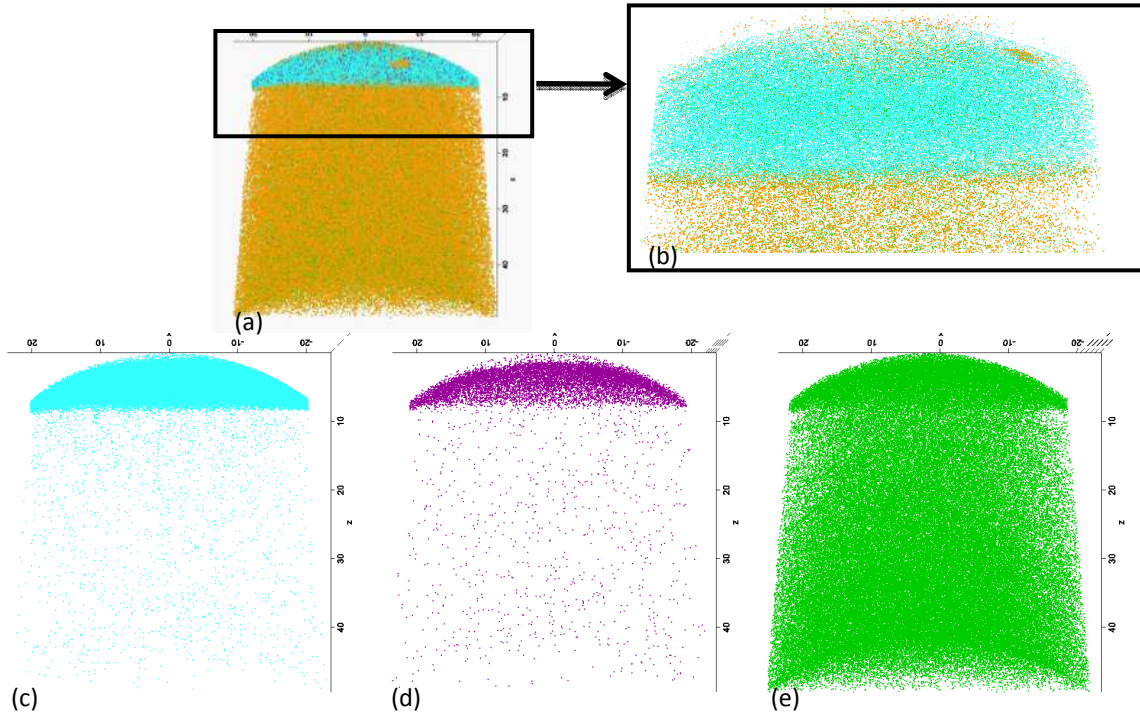


Figure 11. Full 3D Reconstructions of the un-irradiated AlInN/GaN sample. (a) shows the full reconstruction, (b) an up close look of the reconstruction at the interface region, (c) the reconstruction showing only the Al ions, (d) reconstruction showing the In ions only, and (e) the reconstruction showing only the N ions and N compound ions.

A more precise composition analysis can be carried out by considering a rectangular volume along the center vertical z-axis (i.e. growth direction) of the volume shown in Figure 11(a). By looking at the very center of the material we can exclude any surface related non-stoichiometry or artifacts. Figure 12 shows an example of concentration profile obtained in this manner, where “distance” means the distance from the top surface. We can see from the concentration that the region of the GaN spectrum is for the most part stoichiometric (65:35 for the Ga:N) and no Al or In is present. In the upper AlInN layer, we see that In accounted for 2 % and Al nearly 50 % of all atoms in this specimen probed, which means that the top layer was in less indium rich per atom probe measurements than the lattice matched condition of 17 %. Other specimens probed showed a variation of the In:Al stoichiometry, which is not inconsistent with APT being able to analyze a small volume (~100+ nm diameter) that may be smaller than the indium segregation phenomena in AlInN.

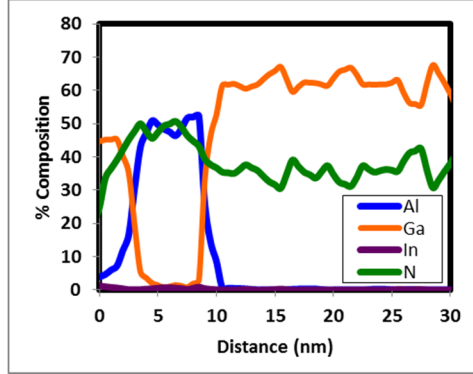


Figure 12. Composition profile as a function of depth in the growth direction, where the individual layers in the AlInN/GaN heterostructure can be identified.

Iso-concentration surfaces or “iso-surfaces” represent internal surfaces around a pixel volume (or voxel) where the concentration of an element is constant. This enables the unique ability to characterize the (chemical) roughness of the buried interfaces, which is something that could not be accomplished by any other technique. To do so, we created an iso-surface of each ion for a specific concentration. We chose the concentration values that represented the value at the interface depth of interest from Figure 12. The voxel size chosen was of 1 nm^3 and the roughness of each iso-surface could be calculated. These are shown in Figure 13. The surface roughness for Al and Ga were similar, 0.227 and 0.232 nm, respectively, while the In roughness was much larger 1.245 nm, which was consistent with the expectation of some degree of indium segregation in indium-containing AlInN. These analyses represented a baseline for us to compare the evolution of the lattice matched AlInN/GaN HEMT structures before and after irradiation.

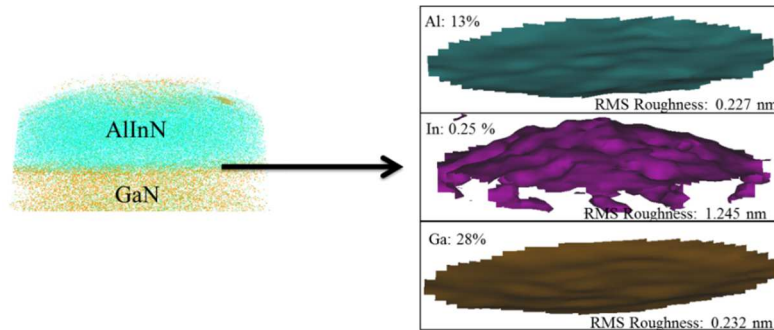


Figure 13. Iso-surface reconstructions of Al, In, and Ga at the un-irradiated AlInN/GaN interface along with corresponding calculated roughness.

2.4.3. APT of Gamma-Irradiated Lattice Matched AlInN/GaN HEMT Heterostructures

Lattice matched AlInN/GaN HEMT heterostructures were then exposed to ^{60}Co gamma radiation up to a total dose of 5.95 Mrad(Si) in order to observe the effects of radiation in the sample. APT specimen preparation followed in the same optimized manner as discussed above and we did not encounter any difficulty measuring them. We do not see any visible difference in the mass spectrum compared to the one in Figure 10 for the un-irradiated sample.

However, differences were observed in the reconstructions for a few of the tips. Figure 14(a) shows the reconstruction for Ga throughout the structure, which revealed an inclusion of Ga from the top surface into the AlInN barrier layer where no Ga would have been expected. This is also visible in Figure 14(c) where Al has been added to the reconstruction, and more dramatically in the Ga iso-surface reconstruction of Figure 14(b). This inclusion was unexpected by the extent (volume) of the inclusion, and because the total dose used are not expected to lead to such movement of atoms.

We have ruled out artifacts of specimen preparation and measurements. Indeed, the Ga in the inclusion did not come from implantation from FIB sample preparation because an analysis of the Ga detected in the inclusion exhibited the natural isotopic distribution (Ga has two isotopes at 69 and 71 atomic mass units) while the Ga ion beam in the FIB instruments used only one isotope (69 amu). Furthermore, the inclusion also contained N and was thus a GaN compound instead of potentially only Ga metal. The mechanisms for this phenomenon are not understood yet and more sampling will be required. However, as we did not observe this in specimens prior to irradiation and transmission electron microscopy measurements carried out of un-irradiated structures did not reveal such phenomenon either, we tentatively think that such inclusion may be caused by exposure to the gamma radiation, potentially as a side effect of the presence of indium.

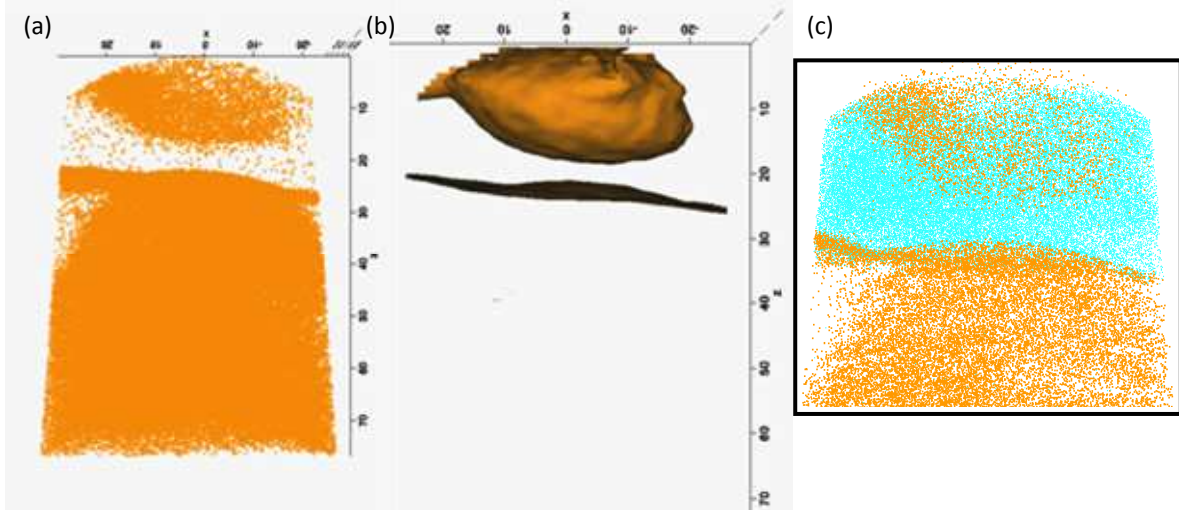


Figure 14. 3D Reconstruction of the irradiated sample. (a) The reconstruction showing the Ga ions only, with the inclusion clearly visible, (b) same as (a) but shown as an iso-surface at a value of 0.28, (c) is an up close look at the inclusion area

Such perturbation of the lattice was also visible in the iso-surface analysis of post-irradiation AlInN/GaN interfaces, as shown in Figure 15 in comparison with Figure 13. The roughness of the interface significantly increased for Al (from 0.227 to 1.185 nm), Ga (from 0.232 to 0.798 nm), and to a lesser extent In (from 1.245 to 1.4 nm). This represented an increase of multiple times for the Al and Ga. The In was already very rough to begin with. This roughening was consistent with expected damage attributed to the exposure to radiation.

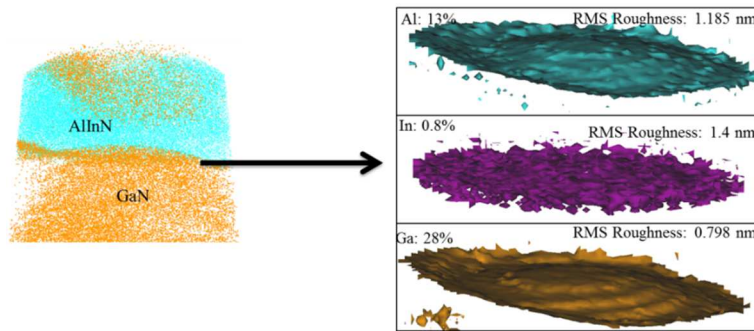


Figure 15. Iso-surface reconstructions of Al, In, and Ga at the post-irradiation AlInN/GaN interface along with corresponding calculated roughness.

2.4.4. Proxigram Comparison of Un-Irradiated and Gamma Irradiated AlInN/GaN HEMT Heterostructures

A more in-depth examination of the HEMT structure heterointerfaces was accomplished by carrying out a proximity histogram (or proxigram) analysis. The process essentially yields an atomic concentration profile in the vicinity of an interface and can therefore provide information on its diffuseness, which could have an impact on the local energy band alignment and thus carrier transport properties. Figure 16 shows the proxigrams, before and after irradiation, for Al and Ga near the isosurfaces that were previously discussed in the AlInN/GaN HEMT and that exhibited significant roughening. The interface, positioned at the center of the graph, did not appear to exhibit much change in its diffuseness, as evidenced by the lack of change in the rising/decaying slope in the proxigram across the interface. The proxigrams did not show a change in diffuseness of the interface after irradiation in all three cases, which was not unexpected because the gamma exposure conditions were not energetic enough to knock out atoms.

In the case of the lattice matched AlInN/GaN structures which showed a larger roughening after irradiation, we have also examined isosurfaces and associated proxigrams at 3 different percentage values of Al (~17%, 27%, and 45%), meaning the surfaces farther from the 2DEG and into the barrier layer. The resulting values of roughness for these before (resp. after) radiation remained essentially the same as for those found earlier, within the 0.05 nm statistical error of our measurements.

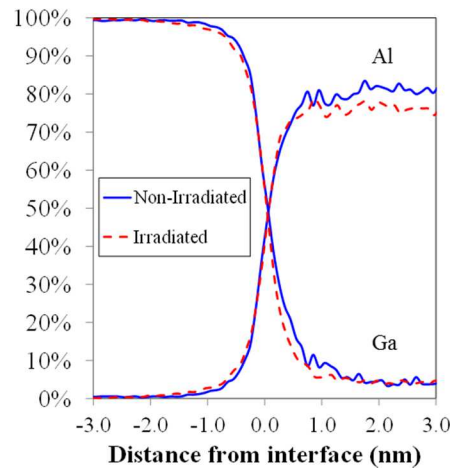


Figure 16. Proximity histogram, before (solid blue line) and after irradiation (dashed red line), for Al and Ga centered at the interface shown in Figure 13 and Figure 15.

2.4.5. APT of Un-Irradiated and Gamma Irradiated Strained AlGaIn/GaN HEMT Heterostructures

Direct comparison with conventional, strained AlGaIn/GaN HEMT heterostructures was performed. The exposure was conducted at the same time as the AlInN/GaN structures, but because of the non-uniformity of the gamma beam, the total dose for the AlGaIn/GaN was 4.52 Mrad(Si) per the dosimetry report. APT specimens were prepared in the same manner and APT experiments conducted under the same optimized conditions. A typical mass spectrum is shown in Figure 17. The main difference with that of AlInN/GaN is the absence of any peak containing In.

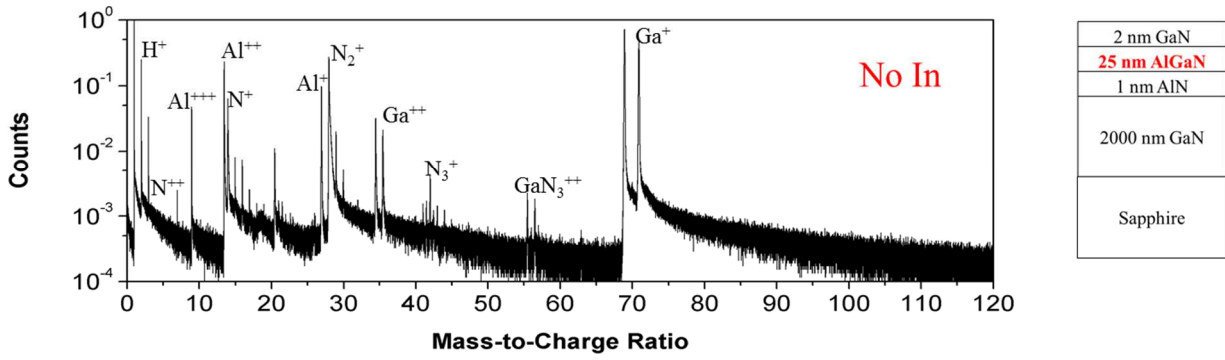


Figure 17. Mass spectrum of the complete AlGaIn/GaN HEMT structure. All the single ions and a few some compound related peaks inherent to GaN field ion emission are visible.

The resulting 3D reconstructions were similar to the one shown in Figure 18(a) prior to irradiation. In it, we can partially discern the upper 2 nm GaN contact layer in orange (faint because the number of Ga ions was small), while the AlGaIn barrier layer is displayed in teal from the combination of Al (blue) and Ga (orange), on top of the GaN buffer layer. After irradiation, no significant change could be observed from these reconstructions (Figure 18(b)) in several specimens probed.

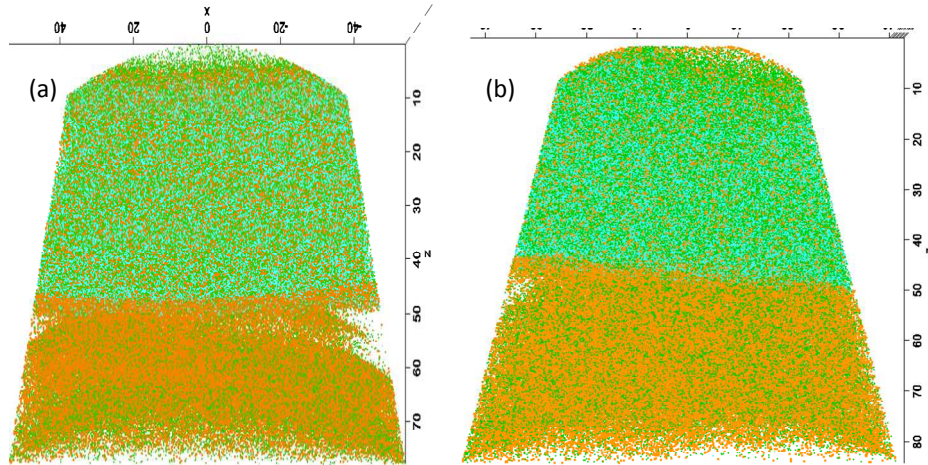


Figure 18. Full 3D Reconstructions of the (a) un-irradiated (b) and ^{60}Co irradiated AlGaIn/GaN HEMT heterostructures.

More quantitatively, composition analysis as a function of depth was conducted by considering a rectangular volume along the center vertical z-axis of the volume, as shown in Figure 11. The exposure to gamma ray was confirmed to not apparently affecting the distribution of elements.

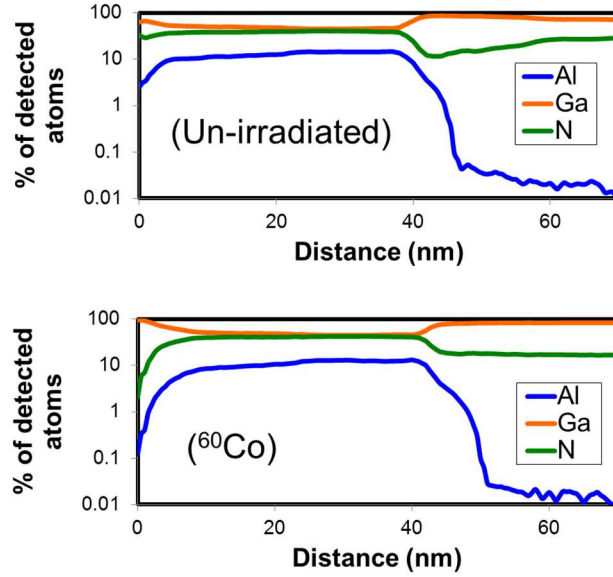


Figure 19. Comparison of composition profile as a function of depth in the growth direction in the AlGaIn/GaN heterostructures prior and after irradiation.

A more precise comparative analysis, utilizing APT iso-surfaces prior and after irradiation, is illustrated in Figure 20. Some degree of interface roughening could be observed after exposure to the total dose of 4.52 Mrad(Si) gamma radiation, with the measured Al increasing roughness from 1.482 to 1.785 nm, and the Ga roughness increasing from 0.943 to 1.519 nm. But this was much less pronounced than in the case of lattice matched AlInN/GaN HEMT heterostructures, which is most likely due to the absence of In and the higher Al amount (Al being a smaller atom than Ga).

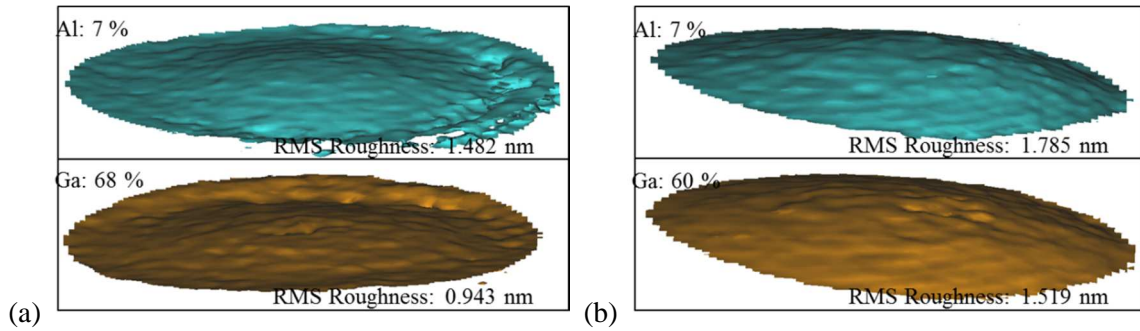


Figure 20. Iso-surface reconstructions of Al and Ga (a) prior and (b) after irradiation near the AlGaIn/GaN interface along with corresponding calculated roughness.

2.4.6. Electrical Characteristics of Un-Irradiated and Irradiated AlInN/GaN & AlGaIn/GaN HEMTs

The electrical transport properties of the AlInN/GaN and AlGaIn/GaN heterostructures were first assessed through room temperature Hall measurements prior and after exposure to the ^{60}Co irradiation, with a total dose of 5.95 and 4.92 Mrad(Si) for AlInN and AlGaIn-based structures respectively. The characteristics of two selected samples are shown in Figure 21.

After irradiation, the lattice matched AlInN/GaN heterostructures demonstrated a 20 % loss in carrier density, although the electron mobility increased slightly. This is consistent with a potential shift in Fermi level as a result of the roughening of the interface near the channel observed in Figure 15. Overall, there is a 8 % decrease in the transport characteristics ($n \times \mu$) of the two-dimensional electron gas. By

contrast, there is minimal change in the case of strained AlGaIn/GaN heterostructures (1~2 % decrease in the $n \times \mu$ product), which is consistent with the higher radiation tolerance observed from APT of those types of structures.

	n_s (cm ⁻³)	μ (cm ² /Vs)	$n_s \times \mu / 10^{13}$
Un-irradiated	2.69×10^{13}	660	1,775
⁶⁰ Co at 5.95 Mrad(Si)	2.17×10^{13}	759	1,647
(a)			
	n_s (cm ⁻³)	μ (cm ² /Vs)	$n_s \times \mu / 10^{13}$
Un-irradiated	1.06×10^{13}	1,395	1,478
⁶⁰ Co at 4.52 Mrad(Si)	1.05×10^{13}	1,385	1,454
(b)			

Figure 21. Comparison of the Hall measurement from two selected AlInN/GaN and AlGaIn/GaN HEMT heterostructures.

Lattice matched AlInN/GaN HEMT devices were able to be processed and irradiated during this first year. The I-V characteristics was shown to degrade as the dose increased for all devices, as shown for one of the HEMTs in Figure 22(a). The maximum drain current degraded by nearly half after exposure to ~5 Mrad(Si). An increase in the pinch-off voltage was generally observed as the dose increased, which suggest the appearance of acceptor-like traps near the channel and is consistent with the decreased carrier density in Hall measurements and could be potentially related to the interface roughness and the inclusions observed in APT. The transconductance of these devices did not degrade much, as illustrated in Figure 23(a), but the main cause of degradation in the device was found to be the gate leakage (Figure 23(b)).

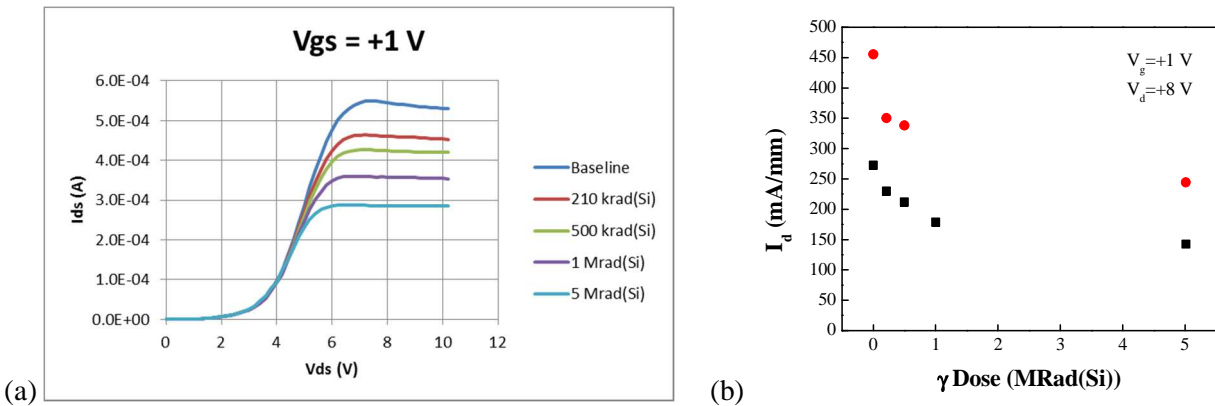


Figure 22. (a) I-V characteristics of AlInN/GaN HEMT devices and (b) maximum drain current as a function of ^{60}Co radiation dose.

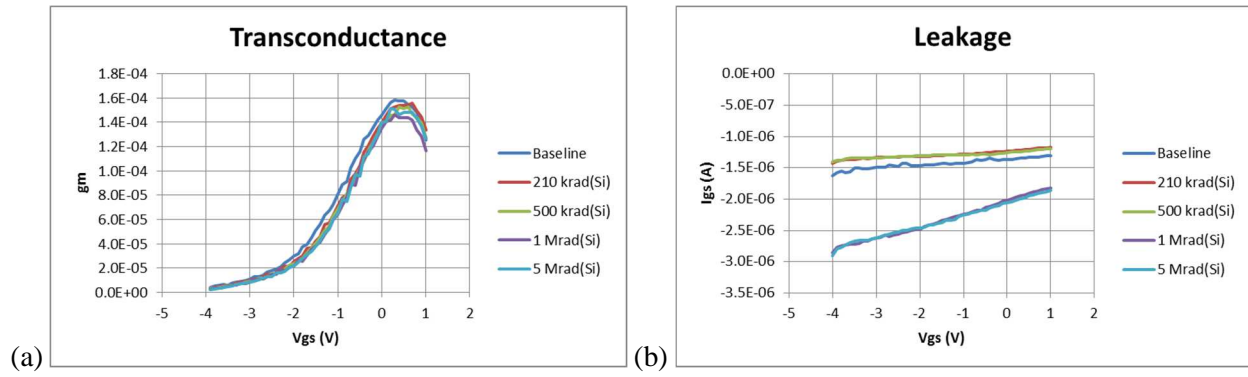


Figure 23. Maximum drain current density in AlInN/GaN HEMT devices as a function of ^{60}Co radiation dose.

2.4.7. Summary

Based on materials and atom probe tomography studies, it appears that AlGaIn/GaN HEMT structures were more gamma radiation tolerant than AlInN/GaN.

2.5. Proton Irradiation of AlInN/GaN & AlGaIn/GaN HEMT Structures

Comparative investigation of the effects of proton irradiation on lattice matched AlInN/GaN and strained AlGaIn/GaN HEMT structures was subsequently carried out. The exposure was conducted by subcontractor Scientific, Inc. using the 2 MV dual source tandem accelerator at Auburn University. The irradiations were done in vacuum at 5×10^{-7} Torr, at room temperature with flowing water cooling of the sample holder fixture to maintain the samples at ~ 55 F. The dose rate was kept constant for each irradiation. The proton beam was scanned over the sample holder. The current was periodically measured using four Faraday Cups upstream of the samples and used to ensure uniformity. The exposure conditions are summarized in the following table.

AlInN/GaN	AlGaIn/GaN	H+ energy	Fluence	Flux
A	A'	500 keV	$1 \times 10^{15} \text{ cm}^{-2}$	1.35×10^{13}
B	B'	2 MeV	$1.1 \times 10^{14} \text{ cm}^{-2}$	2.03×10^{12}
C	C'	2 MeV	$1 \times 10^{15} \text{ cm}^{-2}$	1.35×10^{13}
D	D'	2 MeV	$1.005 \times 10^{16} \text{ cm}^{-2}$	1.02×10^{14}
E	E'	2 MeV		

Table 1. Summary of proton irradiation conditions.

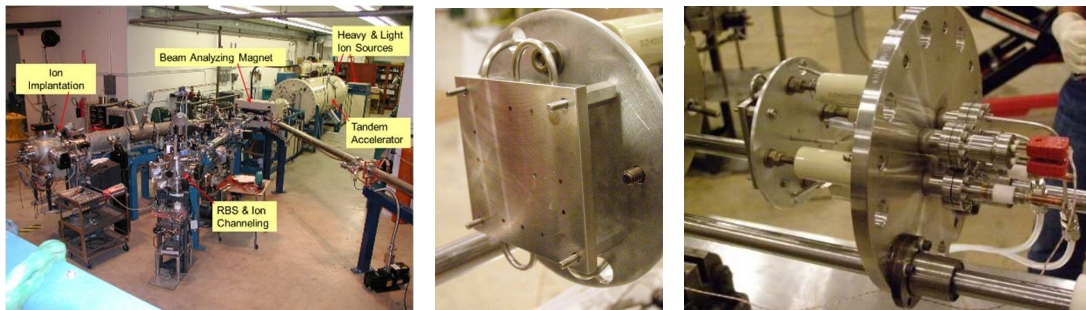


Figure 24. Photographs of the proton irradiation setup used, including water cooling fixture to maintain samples near room temperature.

2.5.1. Design of Proton Irradiation Experiments

The design of experiment included a comparison of the lattice matched AlInN/GaN and strained AlGaIn/GaN transistor structures under the various exposure conditions. Four different conditions were used. A comparison of samples B,C,D (and B',C',D') is expected to lead to insight on the effect of increasing fluence at a fixed 2 MeV proton. A comparison of samples A and C (A' and C') is expected to lead to insight on the effect of proton energy for a fixed fluence, with the expectation that the lower energy irradiation would affect the structure a little bit more. SRIM simulation was performed to estimate the proton depths and energy losses in both conditions, as shown in Figure 25 and Figure 26.

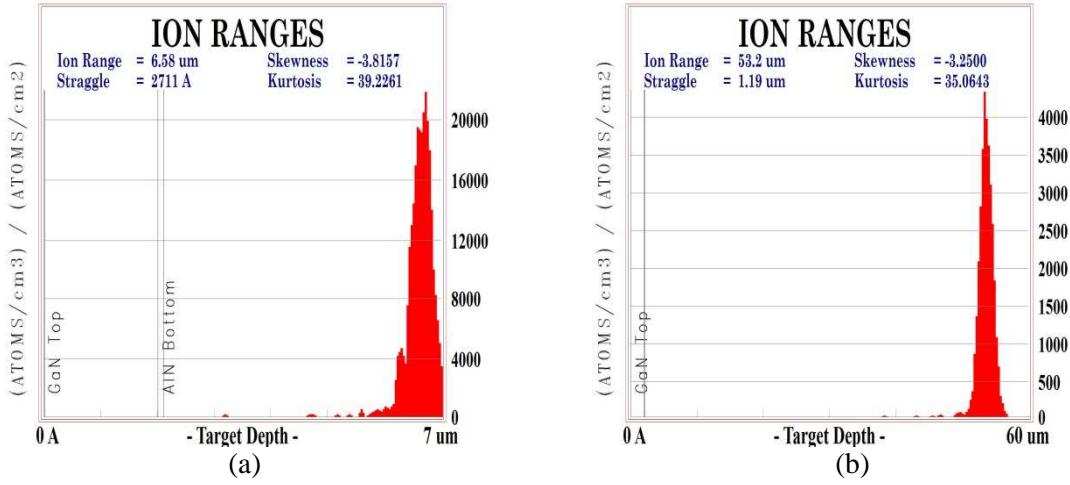


Figure 25. SRIM simulation of ion range for (a) 500 keV and (b) 2 MeV irradiation.

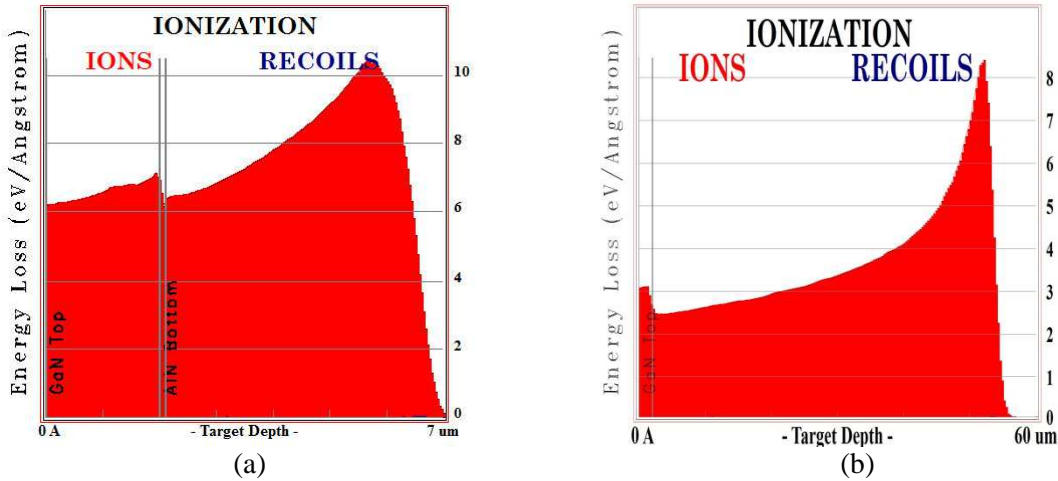


Figure 26. SRIM simulation of energy loss for (a) 500 keV and (b) 2 MeV irradiation.

The samples E and E' were covered with a contact metal (50 nm Au on 50 nm Ti) and had four quadrants each, schematically illustrated below. Half of each sample (two quadrants) included a SiO₂ dielectric layer. Half of each sample in the transverse direction was not irradiated by having it covered with a metal block during exposure. The design of experiment was aimed at investigating the effects of proton exposure on the metal-semiconductor interface, as well as the dielectric-semiconductor interface.

Un-irradiated 50 nm Au / 50 nm Ti / 50 nm SiO₂ / HEMT	2 MeV , 1.005×10¹⁶ cm⁻² irradiated 50 nm Au / 50 nm Ti / 50 nm SiO₂ / HEMT
Un-irradiated 50 nm Au / 50 nm Ti / HEMT	2 MeV , 1.005×10¹⁶ cm⁻² irradiated 50 nm Au / 50 nm Ti / HEMT

Table 2. Schematic of the four quadrants of HEMT structures E and E'.

2.5.2. Effect on Electrical Transport Characteristics of AlInN/GaN and AlGaN/GaN HEMT Structures

The electrical transport properties of the AlInN/GaN and AlGaN/GaN heterostructures were assessed through room temperature Hall measurements prior and after proton irradiation. The resulting sheet carrier density and mobility are shown in Figure 27(a) and (b) respectively, as a function of proton energy and fluence.

We first see in Figure 27(a) that, for AlInN/GaN (black squares), the sheet carrier density decreases monotonically nearly by half with increased fluence up to 10^{16} cm⁻² (at 2 MeV). By contrast, for AlGaN/GaN (red circles), the carrier density remains nearly the same up to a fluence of 10^{15} cm⁻² (at 2 MeV), before decreasing. The behavior is reversed for the mobility. As seen in Figure 27(b), for AlInN/GaN, the mobility remains essentially the same up to a fluence of 10^{15} cm⁻² (at 2 MeV), before sharply decreasing by a factor 3 whereas, for AlGaN/GaN, the mobility decreases monotonically by more than a factor 4.

The scattering of charge carriers out of the 2DEG channel visible from the reduction in carrier density can result from both local changes in the energy band alignment and the formation of charge trap defects. With increasing fluence, it appears that carrier are less scattered out of the 2DEG for AlGaN/GaN than AlInN/GaN. This can be interpreted by the presence of a strong piezoelectric field in the strained AlGaN/GaN heterostructure which can re-inject the scattered carriers into the channel. The decrease in mobility is primarily affected by interface roughness and local potential fluctuation. The fact that the mobility decreases more rapidly in AlGaN/GaN than in AlInN/GaN suggests that a more severe degradation of the surface roughness.

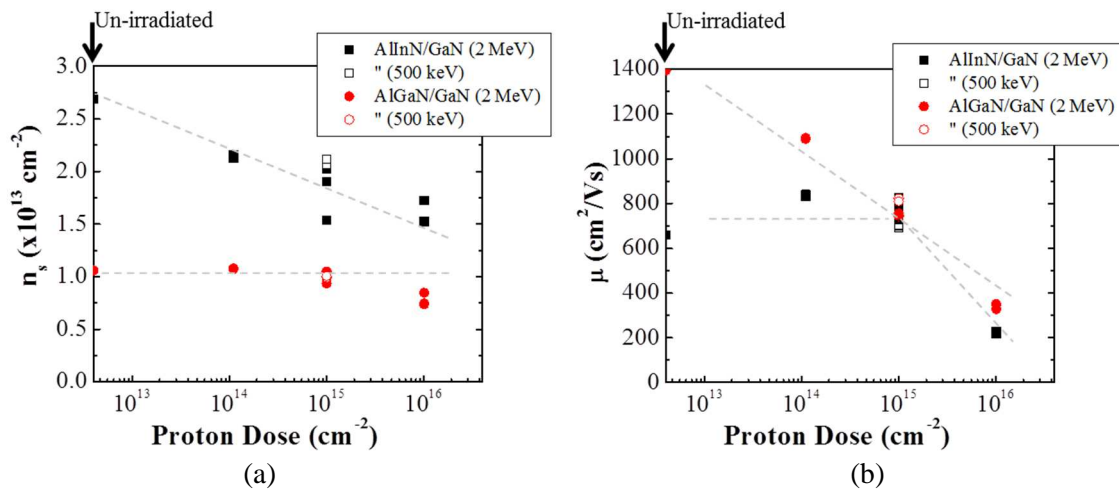


Figure 27. (a) Sheet carrier density and (b) mobility of AlInN/GaN (black squares) and AlGaN/GaN (red circles) HEMT structures as a function of 2 MeV proton dose (solid symbols), and after irradiation under 500 keV proton at 10^{15} cm⁻² dose (open symbols). The lines are guides to the eye.

The combined effect of sheet carrier density and mobility can be seen in their product, which is proportional to sheet conductivity, as a function of fluence in Figure 28. For strained AlGaIn/GaN, the decrease in conductivity is monotonic, whereas there is a sudden drop at a fluence of 10^{15} cm^{-2} (2 MeV) for AlInN/GaN. AlInN/GaN appears more proton radiation tolerant than AlGaIn/GaN up to a fluence of 10^{15} cm^{-2} , while the electrical performance for both drop dramatically beyond that point. The mobility of carriers was found to have a stronger effect than the change in carrier density.

A comparison of the electrical transport characteristics after irradiation with different proton energies (for a fixed 10^{15} cm^{-2} fluence) in Figure 27 and Figure 28, shown as open vs. solid symbols, indicates only a minor influence between 500 keV and 2 MeV for both sheet carrier density and mobility. It thus appears that AlInN/GaN is more proton radiation tolerant than AlGaIn/GaN up to a fluence of 10^{15} cm^{-2} , while the electrical performance for both drop dramatically beyond that point. The change mobility is shown to have a much larger effect than the decrease in carrier density. The thresholds at which the mobility and carrier density start to be affected are also shown to be different for AlInN/GaN and AlGaIn/GaN.

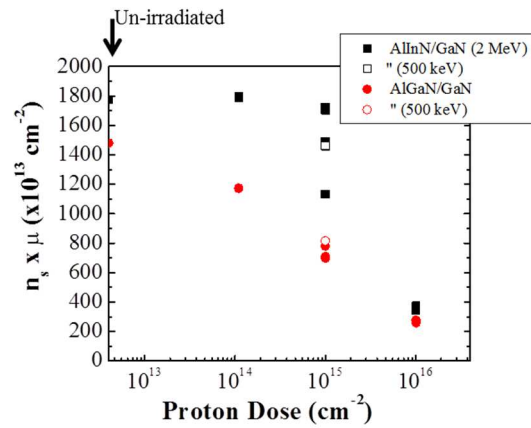


Figure 28. Product of the sheet carrier density and mobility of AlInN/GaN (black squares) and AlGaIn/GaN (red circles) HEMT structures as a function of 2 MeV proton dose (solid symbols), and after irradiation under 500 keV proton at 10^{15} cm^{-2} dose (open symbols).

2.5.3. Atom Probe Tomography Analysis of Proton Irradiated Structures

Preparation and atom probe tomography of numerous specimens from this series of lattice matched AlInN/GaN and strained AlGaIn/GaN HEMT structures were carried out after proton irradiation. We have started by focusing analysis on the highest fluence samples (D and D'). The APT analysis was carried out at 56.3 K using a 532 ps laser pulse energy of 0.4 nJ and pulse rate of 200 kHz. The tip radius was estimated to be 55 nm, with a shank angle of 10 deg.

Typical 3D reconstructions are shown in Figure 29 (top row) for both structures investigated. Although no major effects of the proton irradiation could be seen at that scale, these reconstructions are essential as a routine in order to ensure that we were able to capture the entire heterointerface which is of interest since this is where the 2DEG channel is located. A typical mass spectrum of the entire structure is shown in Figure 29 (bottom row). Such spectrum exhibited the expected emitted ion species for AlInN, AlGaIn and GaN. The absence of unidentifiable peaks in the spectra confirms our current ability to achieve consistent specimens. The only difference between the AlInN/GaN and AlGaIn/GaN HEMTs was in the presence of two indium peaks at amu 115 (In^+) and 57.5 (In^{++}).

Utilizing a central cylinder along the center vertical z-axis, we are able to obtain the concentration profiles along the growth direction shown in Figure 30. In Figure 30(a), the nominal composition of the AlInN was confirmed to consist of 18 % In and 80 % Al for AlInN. Some Ga could be detected, which

most likely came out-diffusion from the chamber during the MOVPE growth process. In Figure 30(b), the nominal composition of the AlGaIn was confirmed to consist of 20-25 % Al and 80-75 % Ga. In both cases, the proton irradiation under exposure condition D was not seen to cause macroscopically observable damage.

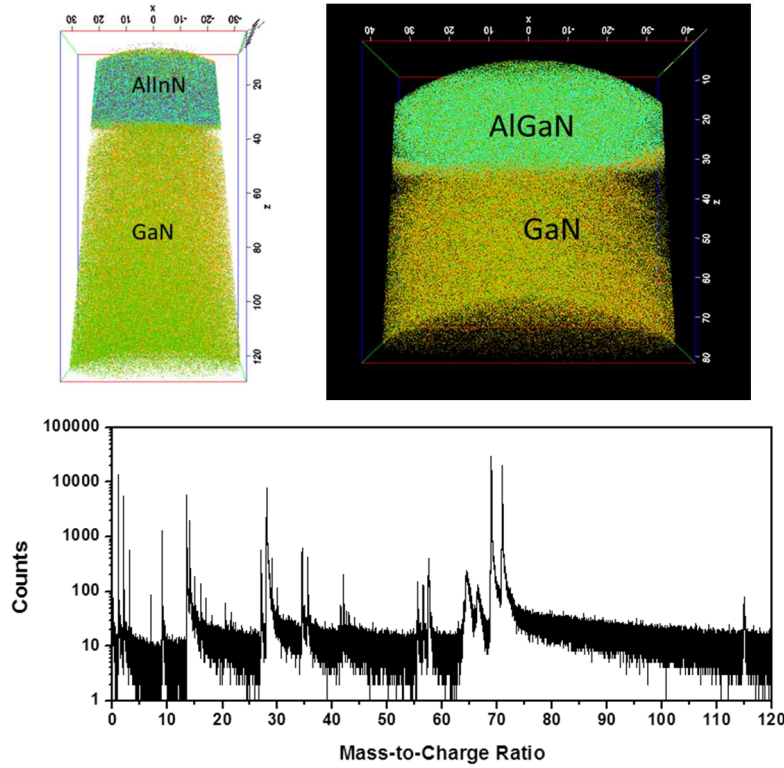


Figure 29. Typical APT 3D reconstructions of (top left) a lattice matched AlInN/GaN HEMT structure D and (top right) a strained AlGaIn/GaN HEMT structure D, both after proton irradiation. (Bottom) typical mass spectrum from a lattice matched AlInN/GaN HEMT structure D.

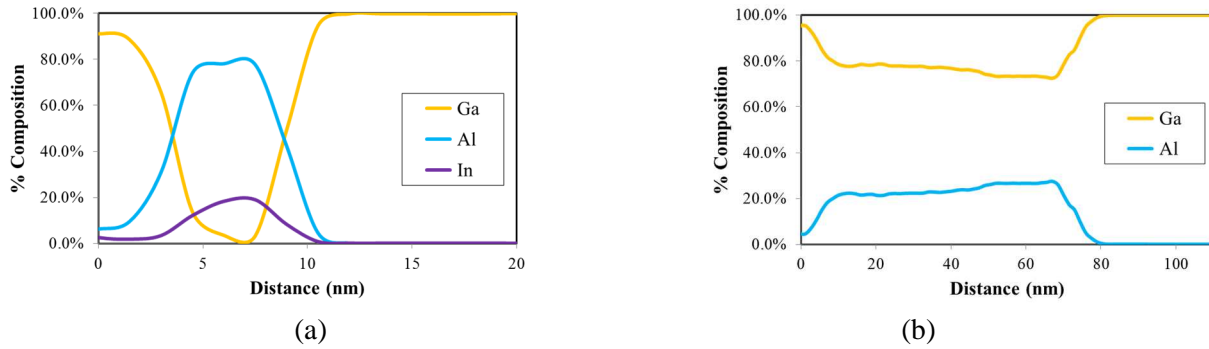


Figure 30. Concentration profiles for (a) lattice matched AlInN/GaN HEMT structure D and (b) strained AlGaIn/GaN HEMT structure D.

Knowing such concentration profiles, we are able to precisely locate the 2DEG channel interfaces in our HEMT structures, as being near where the Al (Ga) concentration starts to increase (decrease), and to construct iso-concentration surfaces (isosurfaces) for roughness analysis. Investigation of the roughness state of this buried heterojunction interface, before and after irradiation, is essential because an increase in this roughness is an indication that the ternary alloy (AlInN or AlGaIn) composition becomes spatially

less uniform near the channel after irradiation. As a result, we can expect local changes in the energy band alignment as well as the potential formation of charge carrier traps, both of which can scatter carriers out of the channel. Because of its ability to resolve chemical composition with high spatial precision, at the atomic layer level, APT is ideally suited to probe such (compositional) roughness of an interface even though it is buried within a structure. This is in contrast to atomic force microscopy, which requires an exposed surface. To do so, we generate 3D iso-concentration surfaces (“isosurfaces”) for elements of interest and utilize the CAMECA Integrated Visualization & Analysis Software (IVAS 3.6.0) to estimate the rms roughness of these surfaces.

For AlInN the isosurfaces in Figure 31(a) were realized at the composition of Al:Ga:In=22:75:3. The measured values of roughness were found to be 0.541, 0.392 and 0.523 nm for Al, Ga, and In, respectively. For AlGaIn, the isosurfaces in Figure 31(b) were realized at Al:Ga=17:83 and yielded value of roughness of 1.749 and 1.805 nm for Al and Ga, respectively. A comparison of the values of isosurfaces roughness between these proton irradiated AlInN/GaN and AlGaIn/GaN HEMT structures and their un-irradiated control samples is shown in Figure 32. A clear roughening is observable in both cases, which is consistent with the drop in mobility seen in Figure 27(b). The rougher interface in the AlGaIn/GaN interface may explain the earlier drop in mobility seen in in Figure 27(b) for AlGaIn/GaN than for AlInN/GaN.

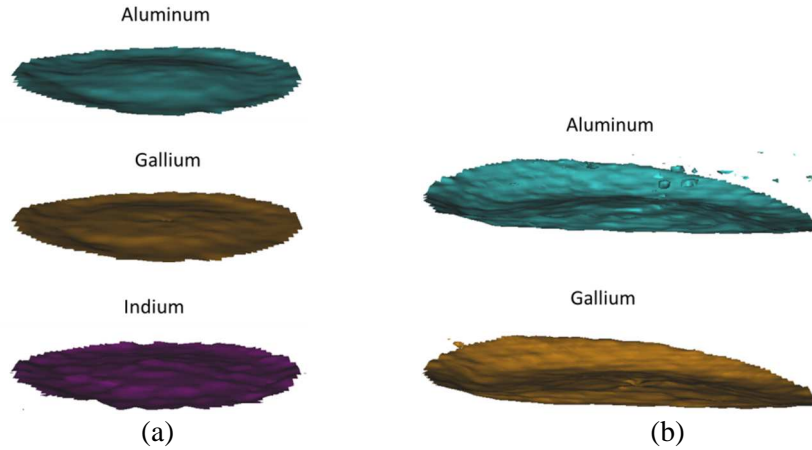


Figure 31. Isosurface reconstructions near the 2DEG channel in (a) lattice matched AlInN/GaN HEMT structure D and (b) strained AlGaIn/GaN HEMT structure D.

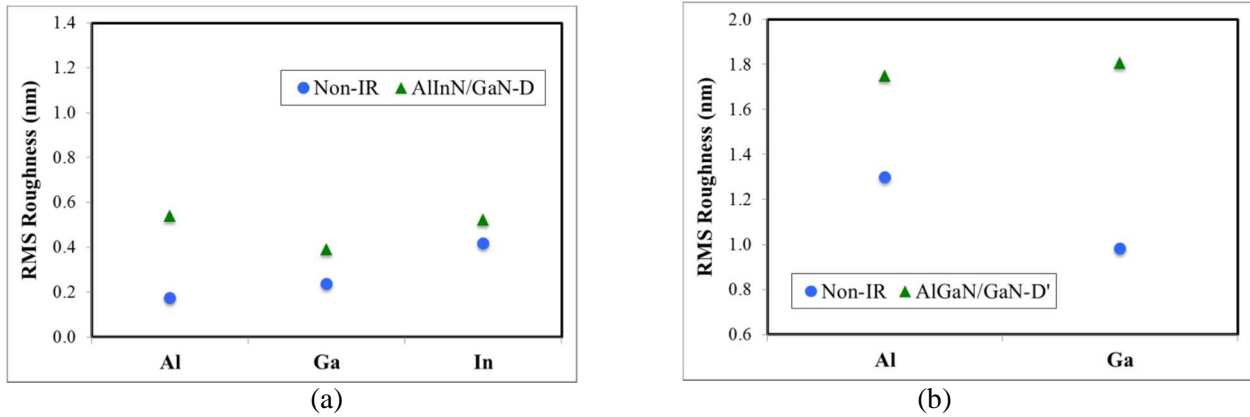


Figure 32. Comparison of values of isosurface roughness for (a) lattice matched AlInN/GaN HEMT structure D and (b) strained AlGaIn/GaN HEMT structure D, with their un-irradiated control samples.

2.5.4. Correlated Analysis of Proton Irradiation on AlInN/GaN and AlGaN/GaN HEMT Structures

Electrical transport vs. atom probe. Figure 31 shows the relative change in heterostructure interface compositional roughness (i.e. between AlInN and GaN, and between AlGaN and GaN) for both HEMT structures compared to their respective un-irradiated baselines and as a function of proton fluence. Values of roughnesses were obtained from the prior isosurface analysis in atom probe tomography. In the inset of each, the trends associated with the 2DEG mobility previously reported for both types of structures are also shown.

In the case of lattice matched AlInN/GaN HEMTs, we observe that the interfacial roughness was always higher than the baseline, whereas the mobility remained nearly constant until a fluence of 10^{15} cm^{-2} . In the case of strained AlGaN/GaN HEMTs, the interface roughness was essentially unchanged for all proton fluences, consistent with a higher structural radiation tolerance of AlGaN based due to a higher bond strength. However, the mobility was found to decrease monotonically with fluence.

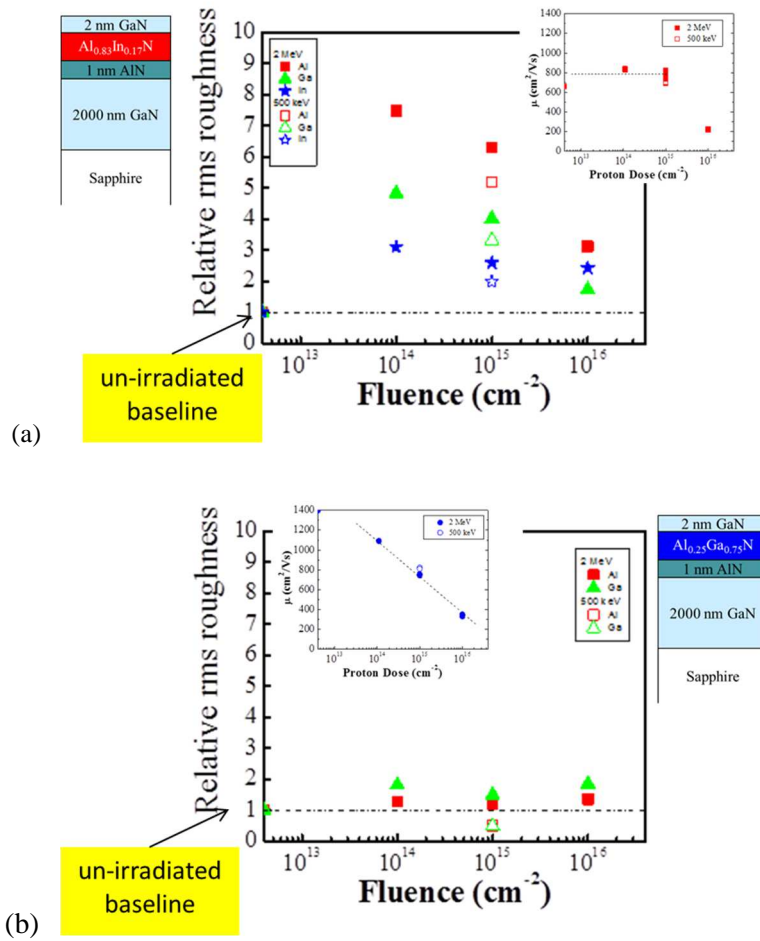


Figure 33. Comparative change in isosurfaces roughness change from the baseline for (a) strained AlGaN/GaN HEMT structures, and (b) lattice matched AlInN/GaN HEMT structures as a function of proton fluence. The insets show the dependence of the mobility as a function of fluence.

Until now, changes in mobility were believed to be due to a combination of interface roughening and fixed charges deposited in the material that scatter carriers when moving in the channel. A major finding here is that the contrasting behavior between mobility and roughness demonstrates proton radiation induced changes in the 2DEG mobility in both AlInN/GaN and AlGaN/GaN HEMTs are not primarily

correlated with interface roughening. Proton irradiation is therefore likely to introduce fixed charges near the channel that scatter carriers during transport.

Electrical transport vs. Raman spectroscopy. One of the objectives of the proposed project was to compare the effects of radiation on the state of strain in AlInN/GaN and AlGaInN/GaN. To do so, we carried out Raman spectroscopy as a function of proton fluence. As shown in Figure 34(a), for AlInN/GaN, no shift in the E₂ (main) Raman peak suggests little change in the state of strain, which would be expected from the lattice matched structure. By contrast, for AlGaInN/GaN, there is a shift toward higher wavenumbers at a fluence higher than 10^{15} cm^{-2} and for energy higher than 2 MeV, suggesting there is strain relaxation (AlGaIn becomes less tensile) at high doses. This is expected to lead to a reduction of the piezoelectric polarization at the AlGaIn/GaN heterointerface, and therefore a lower efficiency at re-injecting scattered carriers back into the channel. And this is exactly what is observed for the sheet carrier density, which starts to drop at the same fluence of 10^{15} cm^{-2} , as shown in the inset of Figure 34(b). In the case of lattice matched AlInN/GaN, even though there is no change in strain, the absence of the piezoelectric field is consistent with the monotonous decrease in carrier density as a function of proton dose.

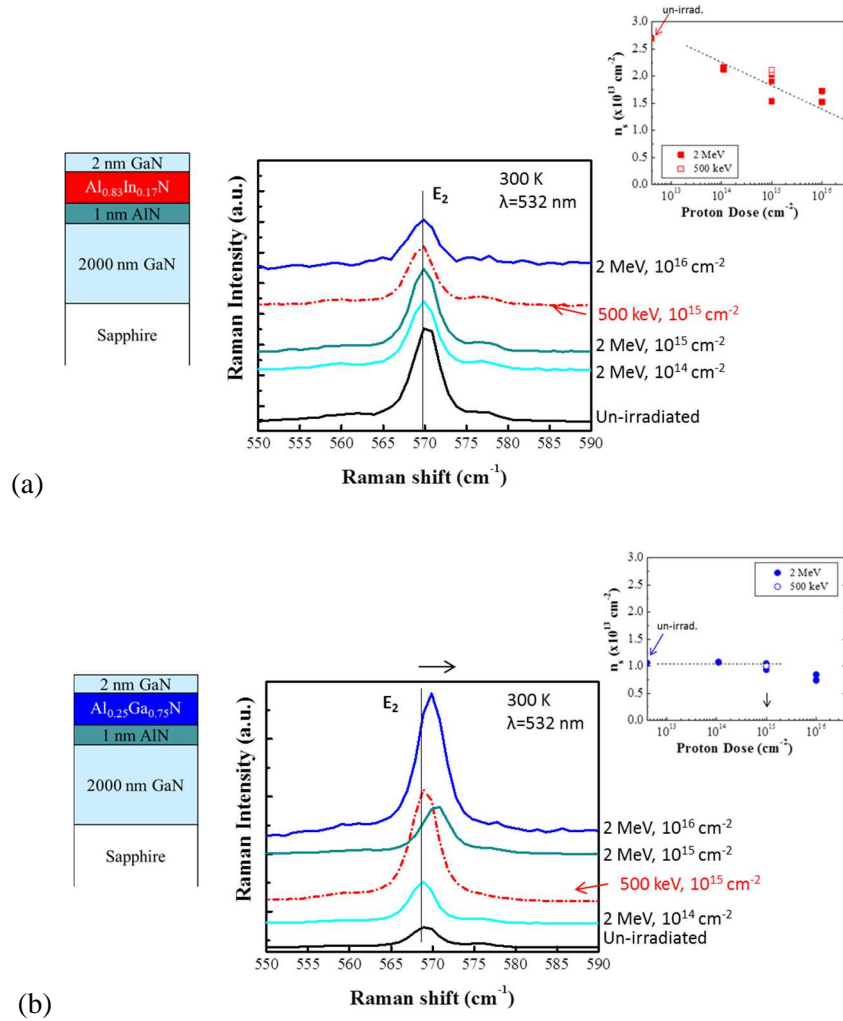


Figure 34. Raman spectra for (a) strained AlGaInN/GaN HEMT structures and (b) lattice matched AlInN/GaN HEMT structures as a function of proton fluence. The insets show the dependence of the sheet carrier density as a function of fluence.

2.5.5. Effect of Room Temperature and Low Temperature Photoluminescence Characteristics

The ultrathin nature of the 2DEG gives an extra advantage because only a small amount of the defects induced from the collisions with highly energetic particles such as protons can affect the electrical characteristics and hence the transistor performances. At the energy studied, most defects are created deep inside the GaN template layer due to the collisions with the irradiation particles. However, the carriers responsible for the photoluminescence from 2DEG are mostly supplied by carrier generation in the GaN flat-band region and successive carrier transfer to the heterointerface, rather than by the direct generation of the carriers near the heterointerface.

We have compared the photoluminescence of proton irradiated AlInN/GaN and AlGaIn/GaN heterostructures as a function of proton energy and fluences. The 300 K photoluminescence spectra of proton irradiated AlInN/GaN heterostructure samples are shown in Figure 35. The Photoluminescence spectra of proton irradiated AlInN/GaN heterostructures samples contain mainly two emission bands: (i) emission from AlInN and (ii) emission from GaN. The decrease of emission intensity is observed with increased of proton energy for the same fluence (A to C) and with increased fluences for the same energy (B, C, D). A similar behavior is also observed in case of AlGaIn/GaN heterostructure samples as evident from Figure 36. This decrease of photoluminescence intensity is associated with increase of nonradiative recombination centers which annihilate the carriers near the band edge for radiative recombination.

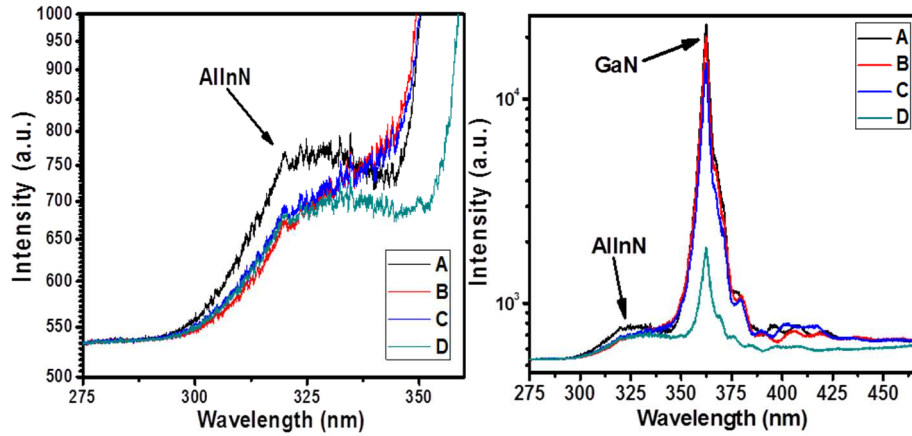


Figure 35. Room temperature photoluminescence of lattice matched AlInN/GaN HMET structures as a function of proton irradiation conditions (A-D).

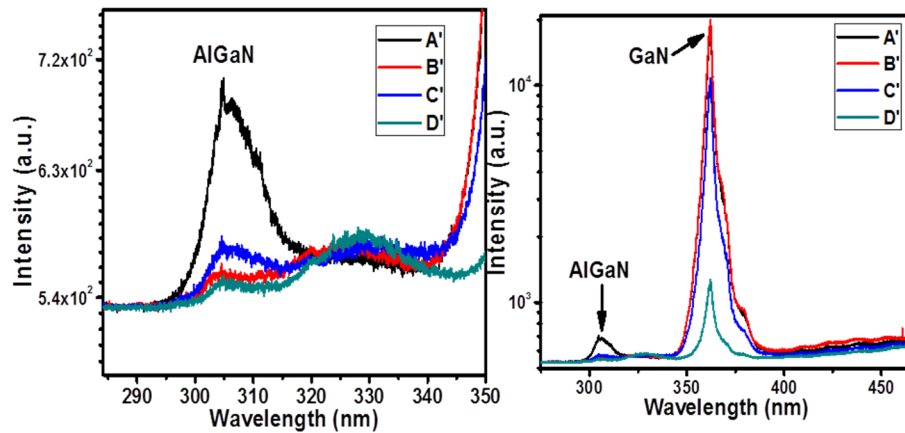
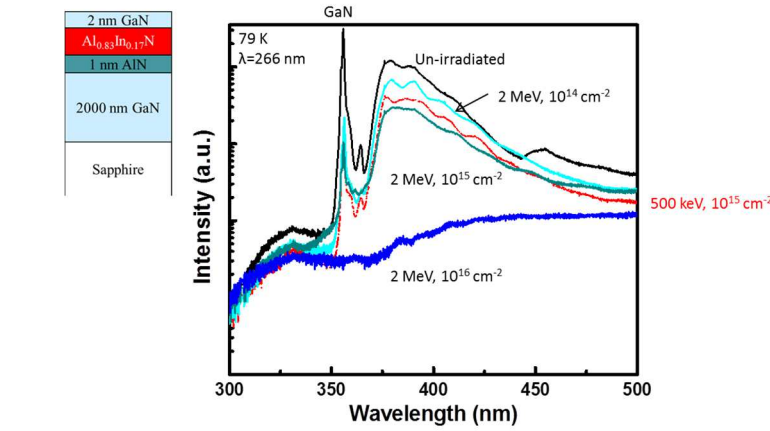


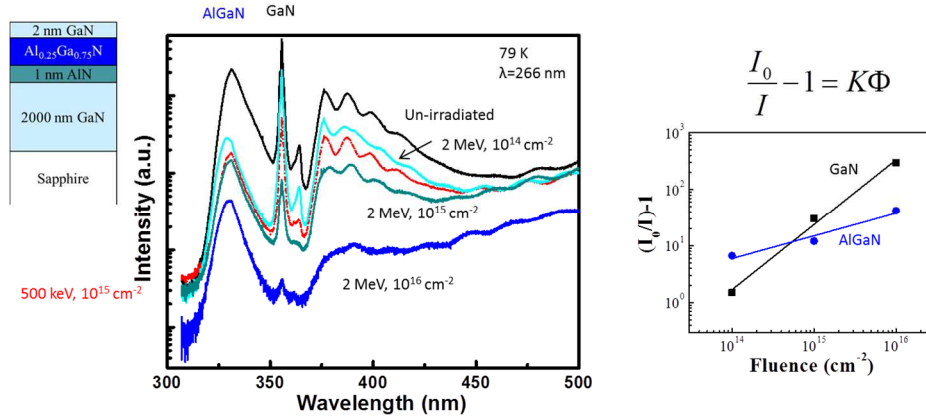
Figure 36. Room temperature photoluminescence of strained AlGaIn/GaN HMET structures as a function of proton irradiation conditions (A'-D').

We have observed significant decrease in the intensity of GaN emission with increase of proton energy and fluences. This indicates that the defects/nonradiative recombination centers are created due to proton irradiation in the GaN layer. Since, the emission of 2DEG is related with the transfer of carriers from the GaN flat-band region, the production of defects in GaN buffer layer due to proton irradiation can significantly affect the 2DEG which acts as channel in HEMTs.

Low temperature (77K) photoluminescence study was subsequently carried out on the samples in order to comparatively probe defects induced by radiation in AlGaInN/GaN and AlInN/GaN HEMT structures (Figure 37). At such temperature, it is possible to better observe luminescence associated with the 2DEG than previously at room temperature.



(a)



(b)

Figure 37. Low temperature photoluminescence emission spectra from (a) lattice matched AlInN/GaN HEMT structure and (b) strained AlGaInN/GaN HEMT structure as a function of proton irradiation energy and fluence.

The main luminescence emission at 365 nm associated with GaN and the 2DEG channel showed a strong decrease in intensity for both. A fit of the function $(I_0/I)-1$ was found to be linear with radiation fluence Φ , where I is the integrated intensity and I_0 the intensity before exposure to radiation, as shown in the case of AlGaInN/GaN in Figure 37(b). A radiation damage constant K can be found to be $1.4 \times 10^{-16} \text{ cm}^{-2}$ could be determined. In the case of photoluminescence intensity for AlGaIn, a sublinear dependence on proton fluence was observed, which is consistent with the expected higher radiation tolerance of AlGaIn compared to GaN due to the higher average chemical bond strength.

No additional or enhancement of deep level related emissions were detected. This shows that the radiation induced defects near the channel are non-radiative in nature. And it is likely that these same defects are also scattering centers that are responsible for the deterioration of the electrical transport characteristics discussed above.

2.5.6. Investigation of Indium Clustering Using APT

One of the unique features of Atom probe tomography is its potential for the analysis of alloy clustering, in particular indium phase separation in the case of AlInN compounds because indium had been reported to form clusters in InGaN due to the dissimilar equilibrium thermodynamic properties of between InN and GaN. In the case of AlInN, InN and AlN exhibit even more dramatic dissimilarities. One of the objectives of the proposed project was therefore to develop this approach to assess whether radiation exposure would increase the level of In clustering in AlInN/GaN HEMT structures. To do so, a large part of this project was to develop a reliable quantitative method to evaluate and compare indium clustering.

We based our model on a threshold for clustering the In distribution on the order of 5 nm. A 100 atom cluster would have a real space linear dimension of approximately 3~4 nm, which is the approximate size of clusters reported via TEM. We have developed two methods in our case by which APT can be used to study non-homogeneous distribution of the alloys in a predefined volume that could be considered as clustering.

The first method utilized was done on AlInN alloys with sufficient thickness and consisted of realizing 2D composition maps in the x-y plane, manually on several specimens. Each 2D map was performed at several positions along the z-direction, with a thickness of 5 nm (Figure 38(a)). In the plane, 1 nm x 1 nm blocks were defined and the atomic density of a chosen element was determined as a function of position x,y,z. Examples of resulting 2D compositions are shown in Figure 38(b).

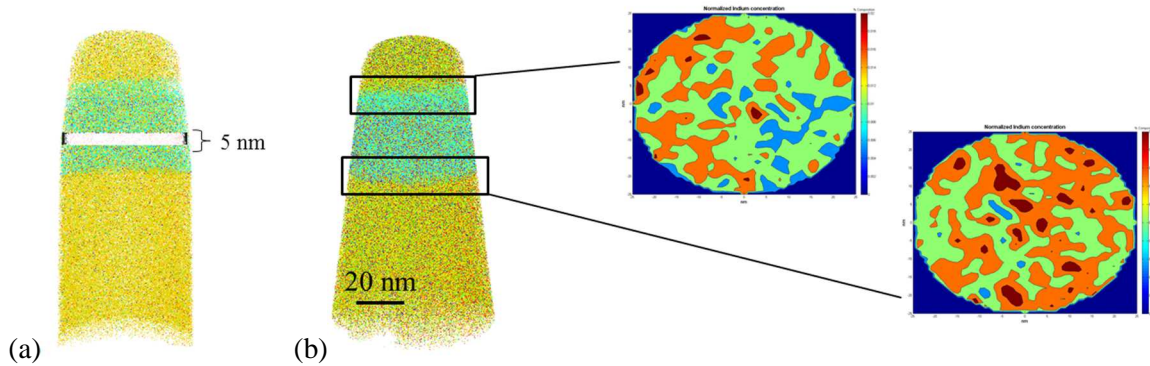


Figure 38. (a) Principle of constructing 2D composition maps. (b) Reconstruction of a typical AlInN alloy specimen studied for indium clustering, with the alloy shown in green while the underlying and top GaN marker layers are shown in more yellowish color. Two representative 2D composition average distributions for indium atoms at the top and at the lower end of the alloy region are also shown.

Although useful, this method remained qualitative. In order to attain a more quantitative analysis, we pursued the determination of binomial distribution in the AlInN alloy. The motivation arises from the fact that, in statistics, a binomial distribution is defined as a probability of getting X successes in N trials in a completely random environment. Therefore, it is expected that composition fluctuations in a homogeneous material should follow a binomial distribution for any random alloy centered on the expected composition. Similarly to the previous qualitative approach, the region of interest (the lattice matched AlInN layer) was divided into predefined size voxels and its concentration measured. In the present case, the layer was divided into voxel sizes of 5 nm x 5 nm x 5 nm cubes; a volume large enough to contain the necessary number of In atoms to deviate from random distribution. The binomial

distribution obtained consist of the frequency distribution of the concentrations obtained for the whole volume. A number of specimens, including before and after proton irradiation, were studied using the binomial distribution method. This has been a time intensive approach, since the AlInN layer was quite thin in the AlInN/GaN HEMT structures studied and therefore the volume was small for each specimen. Figure 39 shows the typical frequency distribution of In concentrations found in the alloy material. The profile did not change significantly following irradiation, remaining essentially similar. Because a good binomial distribution fit centered on a single concentration could be done, we can infer that the alloy was homogeneous with no sign of indium clustering within measurement resolution, either before or after irradiation in our experiments. Evidence of indium clustering would have led to the apparition of two binomial distributions centered on different concentrations, and/or a broadening of the distribution. However, it remains a possibility that higher dose irradiation could lead to more distinguishable indium clustering.

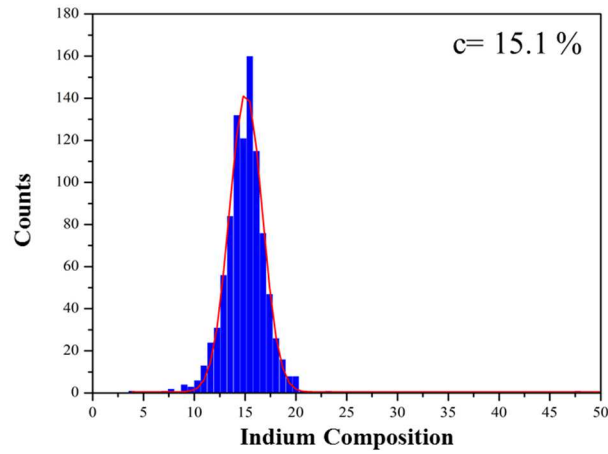


Figure 39. Typical frequency distribution of the indium concentration in AlInN based HEMT structures, with fit to a binomial distribution and the center of the fit is identified as the concentration in the layer.

2.6. Development of Low Temperature AlN Dielectric Passivation Layer

In this project, we have also successfully developed the MOVPE growth of ultrathin (<10 nm) and conformal AlN layers that could be potentially suitable for use as dielectric layers in future AlGaN/GaN and AlInN/GaN HEMTs. AlN offers several advantages over conventional Si_3N_4 dielectric material, as summarized in the following table.

Property	AlN	Si_3N_4
Bandgap (eV)	6.2	~5
Dielectric constant	8.5	7.5
Thermal conductivity (W/cmK)	2.85	0.3

Table 3. Summary of relevant properties of AlN and Si_3N_4 for use as a dielectric.

To do so, we explored the growth parameter space to attain suitable conditions for AlN in our existing MOVPE reactor tool in order to approach the atomic layer deposition (ALD) regime with our available growth capability. One of the constraints for this AlN dielectric layer was to be able to grow it consistently at low temperature (<400 °C). One reason for doing so is to avoid damage to both underlying epitaxial materials and metals that would have been part of the device fabrication. An

additional major advantage of using low temperature AlN is to avoid cracking issues associated with more conventional high temperature AlN. Low temperature presents challenges in terms of parasitic reactions between the trimethylaluminum and ammonia precursors, so low pressure (20 mbar) was optimized and low growth rates were used to minimize such reactions and achieve controllable thicknesses.

Figure 40(a) shows an example of a cross section high resolution TEM (HRTEM) micrograph of the AlInN/GaN HEMT structure shown in Figure 1(a), including the top GaN contact layer, on top of which an ultrathin AlN dielectric layer was successfully deposited. A Ti metallization layer is also visible. Figure 40(b) shows a concentration percentage profile of the elements detected using energy dispersive spectroscopy as a function of the distance along the growth direction (i.e. perpendicular to the interfaces in Figure 40(a)). An approximate thickness of ~5 nm could be estimated from this analysis. From the HRTEM, we could see that the AlN was initially crystalline near the GaN top layer, but its structure became less clear as the layer grew ‘thick’ which was expected from the low temperature growth. The growth rate was confirmed by ellipsometry measurements. Thinner layers of AlN were not clearly distinguishable under HRTEM because of the low contrast with GaN. However, we could visualize thinner AlN layers successfully when grown on other materials (see further below).

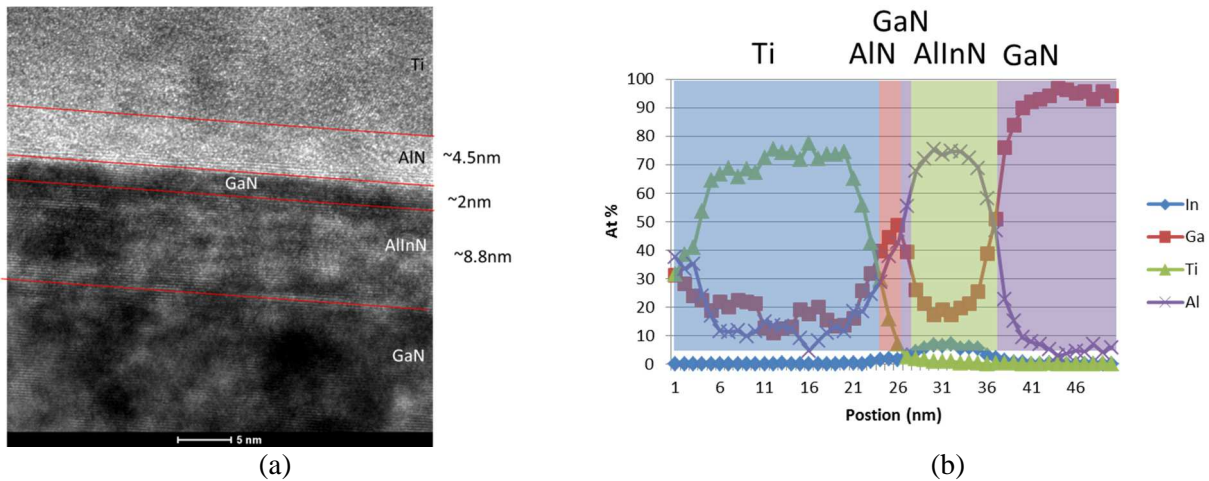


Figure 40. Cross section high resolution TEM micrograph of an ultrathin AlN dielectric layer deposited on the AlInN/GaN structure, along with composition analysis along the growth direction.

Atom probe tomography analysis of such Ti/AlN/HEMT heterointerfaces presented significant difficulty, primary because of the large evaporation field differences between the metal Ti, the dielectric AlN, and the semiconductor HEMT material, as well as their much different physical properties (brittleness and thermal expansion) that come into play when under a high electric field and illuminated by a high power pulsed laser. These often led to early failure. A typical successful run leads to the complex mass spectrum in Figure 41(a) and the 3D reconstruction in Figure 41(b). In particular, the ultrathin AlN dielectric layer could be clearly seen in blue in Figure 41(b).

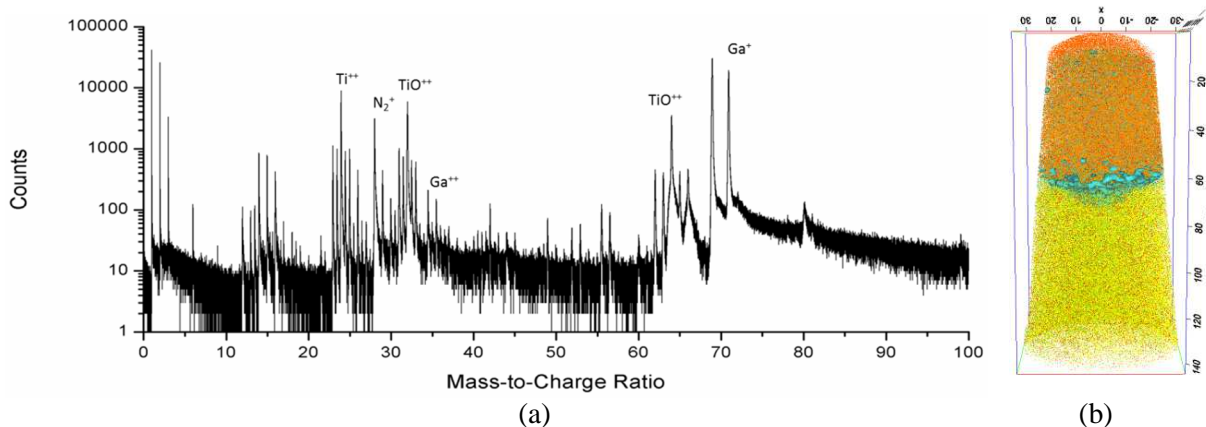


Figure 41. (a) Mass spectrum and (b) 3D reconstruction of the heterointerface between Ti (orange), AlN (blue), and GaN (yellow).

In order to investigate the ability of our MOVPE growth process to approach the ALD process, and therefore its viability, we decided to grow ultrathin AlN layers and demonstrate uniform conformal coverage over high aspect ratio structures. To do so, we utilized a readily available (ZnO) nanowire array, consisting of ~120 nm diameter and several micrometers long. Figure 42(a) shows a typical nanowire on which a ~2nm AlN was conformally grown. Several high resolution images are shown in Figure 42(b) to confirm the thickness uniformity and coverage over large areas.

The low temperature deposition of ultrathin and conformal AlN dielectric layers by MOVPE was therefore successfully developed, which could facilitate their implementation as passivation of future AlGaN/GaN and AlInN/GaN HEMTs, as well as gate dielectric.

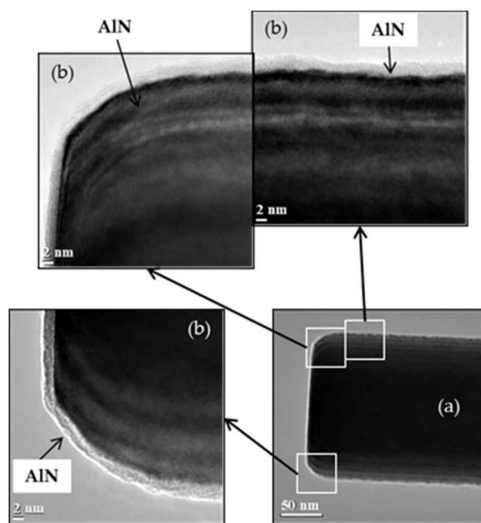


Figure 42. TEM micrographs of an ultrathin AlN layer deposited on a nanowire, demonstrating conformal coverage on large areas with high aspect ratio.

3. IMPACT

3.1. Training and Professional Development

This project partially supported the training, mentoring, and professional development of three graduate students and two postdocs in several aspects of basic research activities, as well as writing journal manuscripts, presenting research results at conferences, and meeting peer researchers.

- Gang Shen completed his Ph.D. dissertation in May 2014 and joined Applied Materials as a semiconductor material process engineer.
- Nabil Dawahre completed his Ph.D. in December 2014 and joined Alta Devices as a device failure analysis scientist.
- Elmer Rivera completed his terminal M.S. Thesis in June 2015.
- Dr. Chin-Jen Chiang has now joined Optoplex where he is a RF engineer.
- Dr. Antaryami Mohanta joined our group after a fellowship at the U.S. Army AMRDEC and has moved on to Purdue University for another postdoc fellowship.

3.2. Dissemination

- N. Dawahre, G. Shen, S.N. Renfrow, S.M. Kim, P. Kung, "Atom probe tomography of AlInN/GaN HEMT structures," *Journal of Vacuum Science and Technology B* 31, 041802 (2013). (this article was one of the JVSTB June 2013 Top 20 Most Downloaded Articles)
- N. Dawahre, G. Shen, S.M. Kim, and P. Kung, "Voltage and laser-assisted mode atom probe tomography of gallium nitride," *Microscopy and Microanalysis* 19 (2013): 990-991.
- N. Dawahre, "Atom probe tomography and spectroscopic analysis of wide bandgap nanostructures," American Vacuum Society 58th Symposium (Nov. 2011).
- P. Kung, "Compound Semiconductor Heterostructures: From Materials to Devices," (invited talk) University of Alabama Huntsville (Nov. 15, 2011).
- N. Dawahre, "Study of Wide Band Gap Semiconductor Structures using Local Electrode Atom Probe Tomography," International Field Emission Symposium (May 2012).
- S. Kim, "Laser assisted atom probe tomography of III-Nitride semiconductors and zinc oxide nanostructures," IEEE Nanotechnology Materials and Devices Conference (Oct. 2012).
- P. Kung, "Atom probe tomography of AlInN/GaN HEMT structures," American Vacuum Society 59th Symposium (Nov. 2012).
- N. Dawahre, "Voltage and laser-assisted mode atom probe tomography of gallium nitride," MSA Microscopy and Microanalysis 2013 Meeting (Aug. 2013).

3.3. Honors and Awards

- Graduate student Nabil Dawahre received a DTRA Basic Research Review Poster Award (Aug. 2012).
- Graduate student Nabil Dawahre received a Best Student Poster Award at the annual meeting for the Microscopy Society of America, the Microanalysis Society (Aug. 2013).
- PI was awarded tenure and promoted Associate Professor (Aug. 2013).
- PI was elevated to IEEE Senior Member status (Nov. 2014).

DISTRIBUTION LIST
DTRA-TR-17-4

DEPARTMENT OF DEFENSE

DEFENSE THREAT REDUCTION
AGENCY
8725 JOHN J. KINGMAN ROAD
STOP 6201
FORT BELVOIR, VA 22060
ATTN: J. CALKINS

DEFENSE TECHNICAL
INFORMATION CENTER
8725 JOHN J. KINGMAN ROAD,
SUITE 0944
FT. BELVOIR, VA 22060-6201
ATTN: DTIC/OCA

**DEPARTMENT OF DEFENSE
CONTRACTORS**

QUANTERION SOLUTIONS, INC.
1680 TEXAS STREET, SE
KIRTLAND AFB, NM 87117-5669
ATTN: DTRIAC